

# **Quantification of myocardial blood flow in small animals with $^{13}\text{N}$ -ammonia microPET imaging**

by

Marc Lamoureux, B.Sc.

A Thesis Submitted to  
the Faculty of Graduate Studies and Research  
in Partial Fulfillment of  
the Requirements for the Degree of  
Master of Science

Ottawa-Carleton Institute for Physics  
Department of Physics, Carleton University  
Ottawa, Ontario, Canada  
Submitted August, 2008

©copyright  
2008, Marc Lamoureux



Library and  
Archives Canada

Published Heritage  
Branch

395 Wellington Street  
Ottawa ON K1A 0N4  
Canada

Bibliothèque et  
Archives Canada

Direction du  
Patrimoine de l'édition

395, rue Wellington  
Ottawa ON K1A 0N4  
Canada

*Your file Votre référence*

*ISBN: 978-0-494-44129-9*

*Our file Notre référence*

*ISBN: 978-0-494-44129-9*

#### NOTICE:

The author has granted a non-exclusive license allowing Library and Archives Canada to reproduce, publish, archive, preserve, conserve, communicate to the public by telecommunication or on the Internet, loan, distribute and sell theses worldwide, for commercial or non-commercial purposes, in microform, paper, electronic and/or any other formats.

The author retains copyright ownership and moral rights in this thesis. Neither the thesis nor substantial extracts from it may be printed or otherwise reproduced without the author's permission.

In compliance with the Canadian Privacy Act some supporting forms may have been removed from this thesis.

While these forms may be included in the document page count, their removal does not represent any loss of content from the thesis.

#### AVIS:

L'auteur a accordé une licence non exclusive permettant à la Bibliothèque et Archives Canada de reproduire, publier, archiver, sauvegarder, conserver, transmettre au public par télécommunication ou par l'Internet, prêter, distribuer et vendre des thèses partout dans le monde, à des fins commerciales ou autres, sur support microforme, papier, électronique et/ou autres formats.

L'auteur conserve la propriété du droit d'auteur et des droits moraux qui protège cette thèse. Ni la thèse ni des extraits substantiels de celle-ci ne doivent être imprimés ou autrement reproduits sans son autorisation.

Conformément à la loi canadienne sur la protection de la vie privée, quelques formulaires secondaires ont été enlevés de cette thèse.

Bien que ces formulaires aient inclus dans la pagination, il n'y aura aucun contenu manquant.



**Canada**

## **Abstract**

Small animal PET imaging is increasingly used to characterize animal models of disease and their therapies *in vivo*. This study aimed to quantitatively evaluate regional uniformity, population variability and test-retest reproducibility of myocardial blood flow (MBF) values in normal rat myocardium using  $^{13}\text{N}$ -ammonia and the Siemens Inveon<sup>TM</sup> small animal PET scanner.

A uniform MBF distribution across the myocardial tissue, small population variability consistent with human data and absolute flow values in the expected normal range were demonstrated and suggest this system is suitable for quantitative, reproducible PET imaging studies in rats. This work also reports, for the first time, an age- or weight-related increase in resting MBF in rats and establishes a normal database of global and regional perfusion values. These values will serve as a reference in detecting significant changes in absolute MBF in the evaluation of therapies for myocardial perfusion in the presence of population and regional variability.

## **Statement of Contributions**

Some of this work was the basis for an oral presentation of an abstract at the Society of Nuclear Medicine's annual meeting in June of 2008<sup>1</sup>. The developed imaging and processing methods including reconstruction parameters and processing parameters were used in two other independent studies in which I have been included in the authorship. The first study, in which I analyzed the PET data and assisted in writing the PET methods and results, investigated the tracking and retention of FDG-labeled stem cells in an ischemic rat model. This work has resulted in abstracts submitted to the American Heart Association Scientific Sessions, the 87<sup>th</sup> Annual Meeting of the American Association for Thoracic Surgery, an accepted abstract at the Canadian Cardiovascular Congress as well as a manuscript submitted to Circulation: Cardiovascular Imaging. The second study, in which I assisted in the data acquisition and preliminary data processing, investigated the altered myocardial metabolism and cardiac function of a mouse model of a genetic human cardiac disease, PRKAG2. This work has resulted in an abstract submitted to the American Heart Association Scientific Sessions and an abstract accepted to the Canadian Cardiovascular Congress. Although the developed imaging methods were used in these studies, the data from these two investigations does not appear in this thesis.

## Acknowledgements

This work is dedicated to my beautiful wife and best friend Laura, who has always stood by my side and without whose support this work could not have been completed. And to my parents, Pierre and Paula, who trusted me to explore my academic interests and curiosities that have led me to where I am today.

I would like to thank my supervisor, Rob deKemp, for his commitment to his students, his impressive ability to create an enjoyable learning environment and for his exemplary leadership, knowledge and guidance throughout this project.

I would also like to thank Stephanie Thorn for her mentorship and tremendous, unconditional commitment to this project in terms of learning and carrying out the microsphere surgeries, method development, animal work and for teaching me tail vein catheterizations.

I am also extremely grateful for the friendship and support of the Image Analysis Team: Tyler Dumouchel for his excellent mentoring and assistance in data acquisition; Jennifer Renaud and Ran Klein for their exceptional expertise in kinetic modeling and development of software; Myra Kordos for her outstanding assistance in animal handling and data acquisition; Samantha Mason and Jeffrey Collins for their patience, flexibility and willingness to provide tracers.

I would also like to acknowledge NSERC, CIHR, HSFO Program Grant and CFI/ORF for funding.

# Table of Contents

<b>Introduction.....</b>	<b>xi</b>
<b>Project Overview.....</b>	<b>xiii</b>
<b>Chapter 1 - Positron Emission Tomography.....</b>	<b>1</b>
1.1 - PET Physics.....	1
1.2 - Coincidence Detection.....	3
1.3 - Data Correction and Image Reconstruction.....	6
<b>Chapter 2 - Tracer Kinetic Modeling of Myocardial Blood Flow with <sup>13</sup>N-ammonia .....</b>	<b>14</b>
2.1 - Overview .....	14
2.2 - PET Tracers .....	14
2.3 - The One Compartment Model.....	16
2.4 - Parametric Imaging.....	21
<b>Chapter 3 - Myocardial Perfusion Imaging: Current Advancements in Humans and Animals .....</b>	<b>23</b>
3.1 - Anatomy .....	23
3.2 - Human Perfusion Imaging.....	26
3.3 - Rodent Perfusion Imaging .....	29
<b>Chapter 4 - Siemens Inveon™ PET Scanner Performance Specifications.....</b>	<b>33</b>
<b>Chapter 5 - Qualitative and Quantitative Imaging of Rat Myocardial Blood Flow with <sup>13</sup>N-ammonia .....</b>	<b>40</b>
5.1 - Imaging Protocol and Analysis Methods.....	40
5.2 - Optimization of Blood Pool Sampling Volume .....	43
5.3 - Relative and Absolute MBF Population Variability .....	47
5.4 - Relative and Absolute MBF Segmental Variability .....	51
5.5 - Perfusion Increase with Weight.....	54
5.6 - Case Study: Detecting Perfusion Changes in the Presence of Population Variability .....	60
5.7 - Test-Retest Reproducibility.....	62
5.8 - Intra-observer Repeatability .....	64
5.9 - Inter-observer Repeatability .....	66
5.10 - Conclusion .....	67
<b>Chapter 6 - Validation of Accuracy using Radioactive Microspheres.....</b>	<b>71</b>
6.1 - Theory.....	71
6.2 - Literature Review .....	72
6.3 - Surgical and Data Acquisition Methods.....	75
6.4 - Results .....	77
6.5 - Conclusion .....	81
<b>Chapter 7 - Rat Myocardial Blood Flow Outside Normal Ranges: Infarct Model ..</b>	<b>82</b>
7.1 - Methods .....	82

7.2 - Results .....	83
7.3 - Conclusion.....	87
<b>Chapter 8 - Conclusions and Future Work.....</b>	<b>89</b>
<b>Appendix.....</b>	<b>92</b>
<b>References.....</b>	<b>94</b>

## List of Tables

Table 1.1 Properties of radionuclides commonly used in PET <sup>6</sup> .....	2
Table 4.1 Properties of scintillation materials commonly used in PET detectors <sup>6</sup> .....	34
Table 5.1 Selected reconstruction parameters used in generating rat perfusion images ..	41
Table 5.2 Processing parameters used in the analysis and modeling of rat perfusion images .....	43
Table 5.3 Summary statistics (mean $\pm$ SD) of LV relative and absolute perfusion values with corresponding CV measurements (n=21). ....	50
Table 5.4 Demographics of Groups 1 and 2. ....	60
Table 6.1 Summary table of microsphere results.....	78

# List of Figures

Figure 1.1 A simplified diagram of a coincidence circuit consisting of amplifiers, pulse height analyzers (PHA) and logical components <sup>6,7</sup> .....	4
Figure 1.2 Types of coincident events including A) True B) Scattered C) Random occurring inside the body and being detected by an axial ring of scintillation detectors .....	5
Figure 1.3 Schematic representation of an annihilation event occurring inside a medium of linear attenuation coefficient $\mu$ at a depth $x$ .....	8
Figure 1.4 Schematic diagram of 16 detectors in a ring and how coincidence events are arranged in a sinogram as a function of $r$ and $\phi$ <sup>6</sup> .....	10
Figure 1.5 An object scanned at all values of $r$ and a single value of $\phi$ yields a projection equivalent to one row in the sinogram $s(r, \phi)$ <sup>6</sup> .....	11
Figure 1.6 Flowchart of the steps involved for general iterative reconstruction .....	12
Figure 2.1 A one compartment model used in perfusion quantification with <sup>13</sup> N-ammonia. ....	16
Figure 2.2 Tissue response given an impulse input function at $t=0$ .....	18
Figure 2.3 Ideal A) blood and B) tissue time activity curves for <sup>13</sup> N-ammonia.....	19
Figure 2.4 A 3D left ventricle (A) can be represented as a 2D polar map (B) corresponding to anatomical segments (C).....	21
Figure 2.5 Representative normalized uptake polar plot and parametric polar plots of $K_I$ , $DV$ and $TBV$ resulting from the kinetic modeling of <sup>13</sup> N-ammonia rat data using FlowQuant <sup>©</sup> and the one compartment model described in the previous section. The bottom panel illustrates typical measured blood (red solid line) and tissue (blue data points) TACs along with the fitted tissue TAC (dark blue solid line) The bottom panel illustrates typical measured blood (red solid line) and tissue (blue data points) TACs along with the fitted tissue TAC (dark blue solid line), the residuals (green dashed line) and the predicted tissue TAC (light blue solid line).....	22
Figure 3.1 A schematic diagram of the four chambers of the heart.....	24
Figure 3.2 A) A schematic drawing of a transaxial slice through the left and right ventricles of the heart. B) A typical transaxial view of a rat heart using <sup>13</sup> N-ammonia.....	24
Figure 3.3 Standard reorientation of the heart in PET imaging to clearly depict the LV. A) SA B) VLA C) HLA.....	25
Figure 3.4 Regions supplied by the coronary arteries as represented in polar map form.....	26
Figure 3.5 A) Illustration of a short axis view of a cardiac rat phantom with the corresponding line profile of measured radioactivity signal across the LV originating from the B) myocardium and C) blood pool indicating spillover into each. ....	31
Figure 4.1 Counts/SD for the first five months after installation. Values below the solid red line indicate the need for maintenance. ....	37
Figure 4.2 System timing resolution for the first five months after installation. Values above the solid red line indicate the need for maintenance. ....	38
Figure 5.1 A representative reconstructed image of a rat heart using <sup>13</sup> N-ammonia	

showing axial slices from the apex (top left) to the base (bottom middle). Coronal and sagittal views are also shown.....	42
Figure 5.2 Time activity curves resulting from four different sampling radii of A) 3.0 mm B) 1.50 mm C) 0.75 mm D) 0.50mm.....	45
Figure 5.3 VLA and HLA slices of a normal rat heart after automatic reorientation showing the appropriately adjusted blood pool sampling volume in the cavity (C), base (B) and atrium (A). The solid line indicates the tissue region sampled. The circles on the tissue are handles for user intervention.....	47
Figure 5.4 Individual polar maps of relative (0-100%, top row) and absolute (0-6 ml/min/g, bottom row) perfusion in the first six subjects to illustrate the variability between subjects and the uniformity in each polar map. Med=median, CV=coefficient of variation.....	48
Figure 5.5 A) Mean uptake and B) mean MBF polar maps across the sampled population (n=21).....	49
Figure 5.6 A) Mean uptake and B) mean MBF polar maps across the sampled population (n=21) divided into five segments (apical, lateral, anterior, septal and posterior). Segmental statistics across the population are shown for C) uptake and D) MBF. * denotes a difference between all other segments and # denotes a difference between the two segments (p<0.05).....	52
Figure 5.7 MBF increase with weight. Errors on the MBF values are derived from the SD between the five segments within each polar map.....	55
Figure 5.8 MBF increase with age. Errors on the MBF values are derived from the SD between the five segments within each polar map.....	56
Figure 5.9 Estimated RC versus Mass (g) .....	58
Figure 5.10 MBF versus estimated RC. Errors on the MBF values are derived from the SD between the five segments within each polar map. ....	58
Figure 5.11 Absolute MBF of Group 1 and Group 2. * denotes p<0.01. Error bars represent Group 1 and Group 2 SD.....	61
Figure 5.12 Bland-Altman plot of test-retest reproducibility (n=9). .....	63
Figure 5.13 Bland-Altman plot of intra-observer repeatability (n=18) .....	65
Figure 5.14 Bland-Altman plot of inter-observer repeatability (n=18) .....	67
Figure 6.1 $^{13}\text{N}$ -ammonia PET derived MBF values (MBF-PET) versus microsphere derived MBF values (MBF-MS). The black line indicates a perfect agreement between methods.....	79
Figure 7.1 $^{13}\text{N}$ -ammonia uptake (A) and MBF (B) polar maps from the three infarct rats .....	84
Figure 7.2 Regions identified as abnormal in Rats 1-3 using A) uptake and B) MBF polar maps. Dark blue colour indicates an abnormal sector as assessed by having a value outside the normal range of the sector mean - 2SD. Light green regions in the apical regions of the uptake maps indicate cropped sectors. ....	86

## **Glossary of Acronyms**

ANOVA - analysis of variance  
CAD – coronary artery disease  
CPS - counts per second  
CR - coefficient of repeatability  
CT - computed tomography  
CV - coefficient of variation  
DG - deoxyglucose  
DQC - daily quality assurance  
DV - distribution volume  
ECG - electrocardiogram  
FBP - filtered back projection  
FDG - fluorodeoxyglucose  
FOV - field of view  
FWHM - full width at half maximum  
HLA - horizontal long axis  
IV - intravenous  
LAD - left anterior descending  
LCX - left circumflex  
LOR - line of response  
LSO - lutetium oxyorthosilicate  
LV - left ventricle  
LVEF - left ventricular ejection fraction  
MBF - myocardial blood flow  
MI - myocardial infarction  
MRI - magnetic resonance imaging  
PET - positron emission tomography  
PHA - pulse height analyzer  
RBF - regional blood flow  
RC - recovery coefficient  
RCA - right coronary artery  
ROI - region of interest  
RPP - rate pressure product  
RV - right ventricle  
SA - short axis  
SD - standard deviation  
SPECT - single photon emission computed tomography  
TAC - time activity curve  
TBV - total blood volume  
VLA - vertical long axis

## **Introduction**

Cardiovascular disease is the leading cause of death worldwide, and in Canada accounting for over 35% of all deaths<sup>2,3</sup>. There is a need for greater understanding of cardiovascular disease, which has prompted the development of animal models of human disease. Most commonly, rodent models of human disease are used because these vertebrate mammals breed quickly, have a short lifetime and share a large portion of the mammalian genome with humans. While other imaging technologies such as computed tomography (CT), magnetic resonance imaging (MRI) and single photon emission tomography (SPECT) have also been adapted for use in small animal research, these provide mainly anatomical data. Molecular imaging with positron emission tomography (PET) in small animals is developing as a powerful imaging tool to study important molecular processes *in-vivo*.

PET is a non-invasive imaging modality that exploits the unique characteristics of positron emitting isotopes chemically attached to biological tracers. When injected into the body, these radioactively-labeled tracers distribute according to their biochemical properties and their emissions can be registered and reconstructed in order to produce a three-dimensional volume of tracer distribution. By generating temporal tomographic images, it is possible to follow the biological tracer's kinetics as a function of time. By applying a suitable mathematical model to this temporal data, information can be extracted pertaining to biochemical processes such as tracer delivery, uptake, trapping, binding affinity or clearance rate.

The applications of PET imaging to non-invasive cardiac studies have been well established since the late 1970s<sup>4</sup> and have become more popular due to the high sensitivity and specificity of PET to detect coronary artery disease (CAD)<sup>5</sup> but limited by high costs and the need for an on-site a cyclotron.

More recently, with the acceleration of genetics research in transgenic animal models, small animal PET has been developing into a powerful tool to non-invasively investigate the molecular and genetic pathways associated with many cardiac diseases and to evaluate therapies *in vivo*.

## **Project Overview**

The objective of this work was to develop and validate PET imaging methods for accurate and reproducible measurements of cardiac perfusion in rodent models of heart disease and to evaluate population variability and test-retest reproducibility within normal populations. These measurements were then used to establish baseline variability in order to be able to accurately detect disease if present. To accomplish this, rat studies were conducted to develop non-invasive imaging protocols that measure blood flow in the heart. These measured values were then tested for repeatability (inter-subjects) and for population variability (intra-subjects) and then compared against invasive, newly developed, ex-vivo measurements. Once the protocols were developed and the population variability had been established, the evaluation of blood flow was tested in rat models of myocardial infarction. These results were then used as pilot data to test the sensitivity of the newly developed imaging protocols in detecting cardiac disease in the presence of normal population variability. Results from this project are anticipated to clarify the mechanism of disease in human patients by serially studying rat disease models *in vivo*. Furthermore, translation of these imaging techniques to other species and ultimately to human studies, is facilitated by a simple scaling of scanner size and radiotracer activity.

# Chapter 1 - Positron Emission Tomography

## 1.1 - PET Physics

When a nucleus possesses an excess of either protons or neutrons, it is energetically unstable and is likely to stabilize by spontaneous radioactive emission. These radioactive decay events primarily include the emission of a photon, alpha particle or beta particle. Positron emission tomography relies on the inherent characteristics of the beta plus emission or the positron decay process in order to accurately detect the spatial distribution of injected radionuclides. The positron has the same mass but opposite charge to the electron and is known to be the electron's antiparticle. The general equation for positron decay from a radioactive atom is shown in Equation 1.1 where  $X$  is the parent atom and  $Y$  is the daughter atom.



As shown in Equation 1.1, the unstable parent nucleus with an excess of protons converts one of its protons into a neutron, positron and a neutrino. The total energy released in this decay is shared between the positron's and neutrino's kinetic energies. This released energy is equal to the difference between the parent and daughter energies minus 1.02 MeV. Therefore, this process cannot occur if the difference between parent and daughter energies is less than 1.02 MeV. The kinetic energy of the liberated positron spans a continuum up to a maximum energy.

Once the positron has been liberated from the nucleus, it loses energy by interacting with the surrounding matter via nuclear and electronic interactions. These interactions not only remove kinetic energy from the positron, but deflect it from its

original path. Once the positron loses most of its kinetic energy, it annihilates with a surrounding electron to produce two 511 keV co-linear photons emitted almost exactly at 180° from each other. Detection of these coincident photons forms the basis of PET imaging. Table 1.1 shows the properties of some radionuclides common to PET in addition to their mean ranges in water before annihilation.

**Table 1.1 Properties of radionuclides commonly used in PET<sup>6</sup>**

Nuclide	E <sub>max</sub> (MeV)	Half-life (min)	Mean Range (mm)
<sup>11</sup> C	0.959	20.4	1.1
<sup>13</sup> N	1.197	9.96	1.5
<sup>15</sup> O	1.738	2.03	2.5
<sup>18</sup> F	0.633	109.8	0.6
<sup>82</sup> Rb	3.40	1.27	5.9

Although the annihilation photons enable the decay event to be localized, there are two fundamental effects that place upper limits on the spatial resolution that can be achieved in PET imaging.

The first effect is positron range. As shown in Table 1.1, the positrons emitted from different radionuclides have different maximum kinetic energies and therefore take longer to dissipate energy to the surrounding matter. This in turn directly affects the mean range. Positron range therefore negatively affects spatial resolution since decay events will be registered with greater accuracy using a nuclide with a smaller positron range such as <sup>18</sup>F.

The second effect that inherently limits resolution is non-colinearity. Although PET imaging assumes that the annihilation photons are emitted exactly at 180°, there is an approximate 0.5° uncertainty due to non-zero momentum of the positrons at annihilation. Depending on the size of the detector ring and therefore the distance the

photons have to travel, non-colinearity can have large implications in the spatial resolution that can be achieved.

## 1.2 - Coincidence Detection

Different from SPECT where physical collimators are needed in order to localize a radioactive decay, PET uses coincidence detection for electronic collimation.

Coincidence detection relies on two high-efficiency radiation detectors and coincidence electronics. If an annihilation event occurs along the line, or more accurately, the volume between the two detectors known as the line of response (LOR), both detectors scintillate and produce an electrical signal. If the signal amplitude on both detectors has the correct energy to be a 511 keV photon and both are detected within a specified timing window ( $2\tau$ ), where  $\tau$  is the timing resolution, it is registered as a prompt coincidence. Figure 1.1 illustrates a simplified diagram of a coincidence circuit.

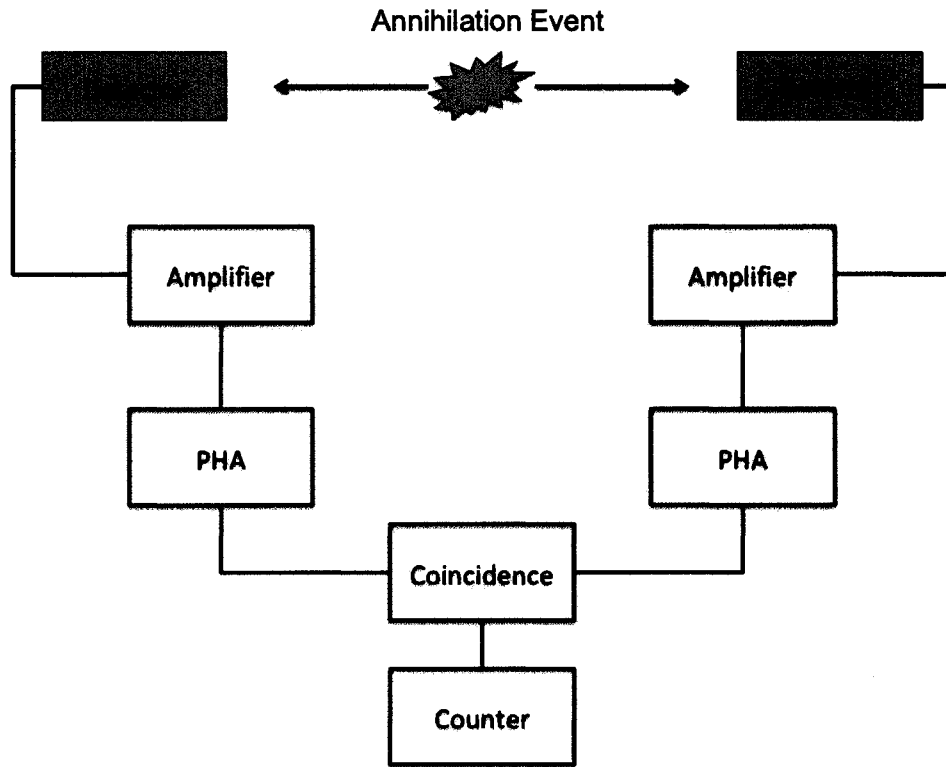


**Figure 1.1 A simplified diagram of a coincidence circuit consisting of amplifiers, pulse height analyzers (PHA) and logical components<sup>6,7</sup>**

As illustrated in Figure 1.1, electrical signals are amplified from the detector crystal into pulse height analyzers which resolve the energy of the incident photon. If the energy falls within a specified energy window, a logical signal is sent to the coincidence detection stage. If two pulses are received within a  $2\tau$  window, then a logical signal is sent and recorded as a prompt coincidence along the LOR between the two specific detectors. Typical PET systems contain multiple detectors arranged in a ring around the field of view (FOV) and are extended axially to acquire multiple image slices to form a three-dimensional volume and to obtain oblique coincidence events between different axial rings. On most modern PET systems, coincidence events are recorded in list-mode format. List-mode is a raw format in which among other data, each event's precise time

and LOR is recorded so that the events can be arranged into time bins after the completion of the PET scan.

Ideally, all coincidences should reflect the true distribution of radionuclides within the FOV, however, there are other types of coincidences that have confounding spatial information and introduce bias and noise into the image. These other types of coincidences include random and scattered coincidences. Figure 1.2 illustrates all three types of coincident events.

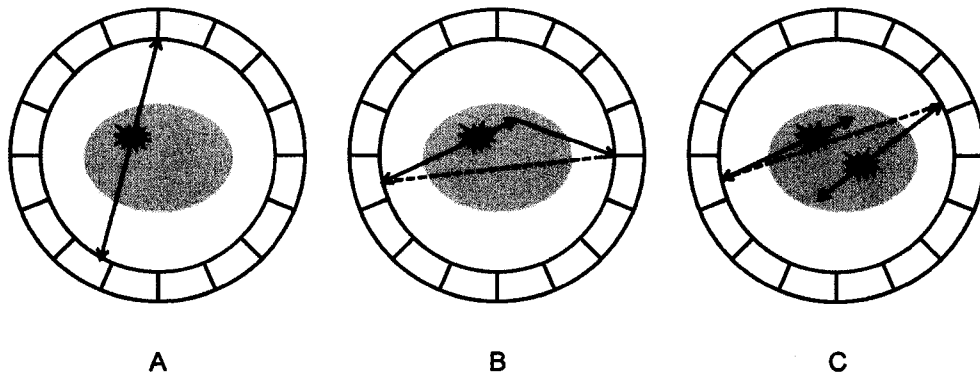


**Figure 1.2 Types of coincident events including A) True B) Scattered C) Random occurring inside the body and being detected by an axial ring of scintillation detectors**

In scattered events, one or both photons undergo Compton scatter, either in the body or in the detector, changing its original path. This deflected photon still gets registered in coincidence with its corresponding photon, however, the event is registered in the wrong LOR introducing background signal in the final image, reducing contrast.

In random coincidences, uncorrelated photons originating from different annihilation events get detected within the finite timing window and therefore get registered as a coincidence along an incorrect LOR. Increasing the timing window will therefore increase the number of random coincidences accepted.

In the non-ideal cases where scattered and random coincidences occur, photon interactions occur within the body and incorrect spatial information is acquired. The next section describes how the data is corrected for detector efficiency, randoms, scatter and attenuation before being reconstructed into a fully three dimensional image.

### **1.3 - Data Correction and Image Reconstruction**

Before an image is reconstructed into a fully three dimensional volume, the data is typically corrected for isotope decay, detector efficiencies, scattered and random events, as well as photon attenuation.

To correct for varying individual detector efficiencies, a uniform radioactive source is scanned over a long period of time in order to measure, with minimal noise, relative efficiencies in detecting coincidences along all the LORs in the system. These measured efficiencies that include the geometrical variations, physical dimensions and electronic differences between detectors are then used as a multiplicative factor to each LOR in the system before image reconstruction to ensure accurate correction of sensitivity variations among all detectors.

To correct for random coincidence events, two methods exist and are typically performed in real-time during data acquisition. It can be shown that estimation of the rate of random coincidences ( $N_R$ ) in a pair of detectors is:

$$N_R = 2\tau N_1 N_2 \quad (1.2)$$

where  $N_1$  and  $N_2$  are the photon detection rates on the paired detectors 1 and 2 and  $2\tau$  is the coincidence timing window. In the first method for randoms correction, the number of randoms given by Equation 1.2 can be subtracted from the total number of coincidences registered by detectors 1 and 2. This first method would require additional

electronics to monitor the single photon rates on all detector elements. Another method, the most commonly implemented randoms correction, is known as the delayed coincidence window technique. In this method, random coincidence events are measured by adding a second coincidence circuit between detector pairs, but delaying one of the logic pulses in time by several  $\tau$ . This ensures that the detector pair cannot detect any true events and therefore directly measures the random rate. The random coincidences are then subtracted from the total coincident events in the LOR to complete the randoms correction.

Although many data corrections such as random corrections and detector efficiencies are needed at the detection stage, the annihilation photons also undergo substantial interactions in tissue that degrade image quality even before reaching the detector ring. At 511 keV, photons interact with matter primarily through Compton scattering and the photoelectric effect. Specifically, within human or animals that consist of soft tissue and bone, 511 keV photons primarily interact via Compton scattering<sup>8</sup>. In Compton scattering, an incident photon elastically scatters off a free or loosely bound atomic electron, changing its direction. It can be shown that the energy of the scattered photon is:

$$E_s = \frac{mc^2}{\frac{mc^2}{E} + 1 - \cos\theta} \quad (1.3)$$

where  $E_s$  is the energy of the scattered photon,  $mc^2$  is the rest energy of the electron,  $E$  is the energy of the incident photon and  $\theta$  is the scattering angle.

The most common method to correct for photon scattering in PET is simulation-based. Using the emission data and the subject's geometry, scatter is estimated using a

simple single scatter model employing the Klein-Nishina probability function<sup>9</sup>. The scattered events are then subtracted from the emission data to produce a scatter corrected image.

As a result of the interaction with matter, the primary annihilation photons become attenuated from their original path. This process is given by:

$$I(x) = I(0)e^{-\mu x} \quad (1.4)$$

where  $I(x)$  is the intensity after traversing  $x$  cm of material,  $I(0)$  is the initial intensity and  $\mu$  is the linear attenuation coefficient in  $\text{cm}^{-1}$ . It is evident from Equation 1.4 that photons that originate deeper within tissue will be more attenuated. To correct for attenuation in PET, consider a uniform tissue with linear attenuation coefficient  $\mu$  with a point source located at a depth  $x$  as shown in Figure 1.3.

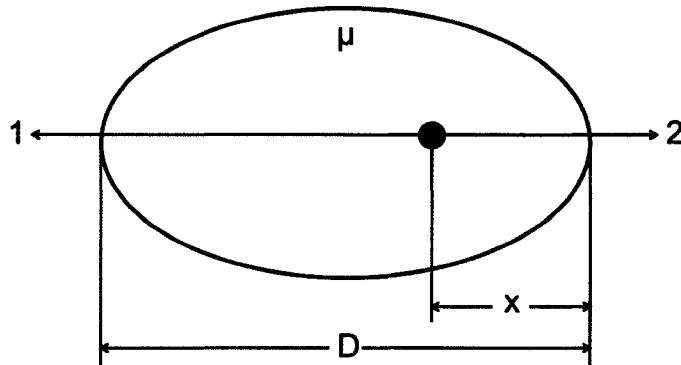


**Figure 1.3 Schematic representation of an annihilation event occurring inside a medium of linear attenuation coefficient  $\mu$  at a depth  $x$**

Given Equation 1.4, the probabilities of photons 1 and 2 escaping the tissue along their respective original paths are

$$p_1 = \frac{I(D-x)}{I(0)} = e^{-\mu(D-x)} \quad (1.5)$$

$$p_2 = \frac{I(x)}{I(0)} = e^{-\mu(x)} \quad (1.6)$$

Since PET relies on coincidence detection, the probability of detecting these two photons in coincidence is therefore their product:

$$p_{\text{coincidence}} = p_1 p_2 = e^{-\mu(D-x)} e^{-\mu(x)} = e^{-\mu D} \quad (1.7)$$

From Equation 1.7, it is clear that the attenuation seen by the PET detector ring does not depend on the depth of the annihilation event, but solely on the attenuation coefficient across the subject along the entire LOR between both detectors. By this principle, attenuation correction can be either calculated for uniform and geometrically simple objects or measured experimentally. To measure attenuation, transmission sources such as  $^{68}\text{Ge}$ ,  $^{137}\text{Cs}$  or  $^{57}\text{Co}$  rotated around the subject, outside the tissue, can be used to generate transmission data to correct for attenuation by simply taking Equation 1.4 and multiplying by the inverse of Equation 1.7. More recently, dual modality PET scanners that include a CT capability are being used due to the high statistical quality, speed, and high spatial resolution of CT transmission images.

Before image reconstruction can proceed, LOR data must be arranged into projection data known as a sinogram. Sinograms are functions of  $r$  and  $\phi$  as shown in Figure 1.4. Sinograms are two or three dimensional matrices in which each element consists of the number of coincidence events detected by the corresponding detector pair as defined by  $r$  and  $\phi$ . For the purposes of this section, only two dimensional sinograms will be discussed. Each row in the sinogram represents a projection of the image across all  $r$ 's at a specific angle  $\phi$ .

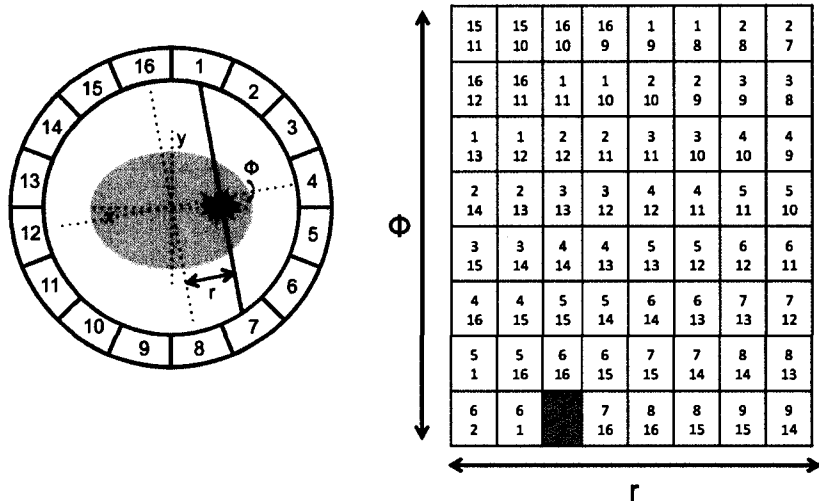


**Figure 1.4 Schematic diagram of 16 detectors in a ring and how coincidence events are arranged in a sinogram as a function of  $r$  and  $\phi$ <sup>6</sup>**

After rebinning the LOR data into projection data and incorporating all the data corrections previously mentioned, PET data can then be reconstructed into an image plane or image volume using various techniques. The first and most basic reconstruction technique is known as filtered backprojection (FBP). To reconstruct and image using FBP, projection data at one angle  $\phi$  (one row in the sinogram) is used at a time as shown in Figure 1.5.

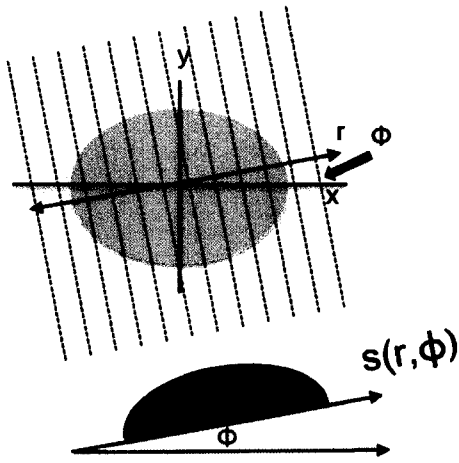


**Figure 1.5** An object scanned at all values of  $r$  and a single value of  $\phi$  yields a projection equivalent to one row in the sinogram  $s(r, \phi)$ <sup>6</sup>

The one dimensional Fourier Transform is applied in  $r$  and the result multiplied by a filtering function in frequency space. This filtering function can take on multiple shapes, however, a ramp function in frequency space amplifies high spatial frequencies and is commonly used to compensate for less sampling at higher frequencies<sup>10</sup>. The inverse Fourier Transform is then applied and the filtered result is backprojected back into the spatial domain. This process is repeated for all angles (rows) in the sinogram to produce the final, filtered, reconstructed image.

With the advancement of computing power, another technique for image generation known generally as iterative reconstruction has become increasingly popular due to its improvements in signal-to-noise, spatial resolution and its ability to incorporate a model of the imaging system<sup>6</sup>. Although the detailed explanation will not be covered due to the complexity of the technique, all iterative reconstructions compare the measured data to an estimate and update the estimate until convergence between the

estimate and the measured data is reached. Figure 1.6 illustrates the general flow describing the iterative reconstruction technique.

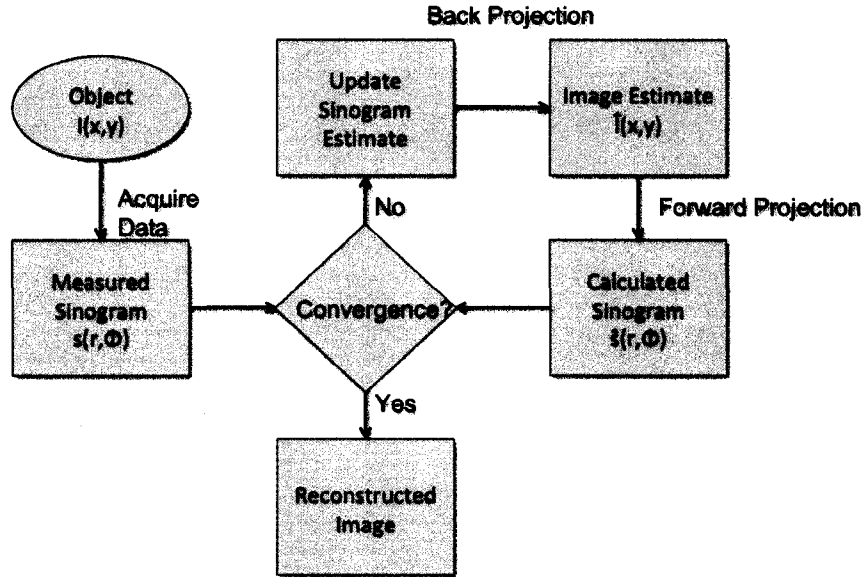


**Figure 1.6 Flowchart of the steps involved for general iterative reconstruction**

As shown in Figure 1.6, data is acquired and rebinned into a measured sinogram. This measured sinogram is then compared with a forward projected initial estimate of an image. In the forward projection step, most reconstruction algorithms use system models of geometry, scatter, positron range etc. to simulate the imaging system and to produce more accurate reconstructed images. If the two sinograms do not agree after forward projection, the estimated sinogram is updated, backprojected, forward projected and compared to the measured data again. This process repeats itself until the cost function, that gives a measure of the difference between the estimated and calculated sinograms, is minimized<sup>6</sup>. Once the measured and calculated sinograms reach convergence, the image is ready for analysis.

To obtain a quantitative image in units of activity concentration instead of count density, a calibration factor must be used to scale the reconstructed image. This calibration factor is found by scanning a uniform phantom with a known activity concentration and relating the count density within this phantom to its activity concentration. The calibration factor is typically incorporated in the data correction steps resulting in reconstructed images with units of Bq/cc.

## **Chapter 2 - Tracer Kinetic Modeling of Myocardial Blood Flow with $^{13}\text{N}$ -ammonia**

### **2.1 - Overview**

Due to the functional and not solely anatomical nature of PET data, reconstructed images are typically only the starting point for various image analysis techniques. In the first chapter, PET was described as an imaging modality that detects the spatial distribution of radioactive nuclei. Although this is true, in many cases, the radioactive nuclei are chemically incorporated into molecules of biological interest, known as tracers that are usually injected intravenously. The kinetic modeling of these injected tracers allows for the tracking of their distribution, absorption and clearance. In order to track the radiotracers in time and to get quantitative measurements of biological processes, dynamic PET sequences in which the image data is sampled and binned versus time are used to produce temporal as well as spatial data. This dynamic data can then be used in a mathematical model. The purpose of a mathematical model is to develop a relationship between the true physiological parameters and the measured PET data and to account for all the biological factors contributing to the PET image. In this chapter, an overview of common PET tracers will be presented along with a specific mathematical model used in order to assess absolute myocardial blood flow and its advantages related to parametric imaging.

### **2.2 - PET Tracers**

Many different PET tracers have been developed in order to study the uptake, delivery, trapping or binding of certain biological compounds. Some of the more

common tracers include  $^{18}\text{F}$ -labeled fluorodeoxyglucose (FDG),  $^{11}\text{C}$ -labeled acetate,  $^{13}\text{N}$ -labeled ammonia,  $^{82}\text{Rb}$  and  $^{15}\text{O}$ -water. FDG is the most commonly used tracer in PET imaging and is a chemically synthesized glucose analogue that is used to measure tissue glucose utilization since both glucose and deoxyglucose (DG) utilize the same glucose transporter to cross the cellular membrane. Once inside the cell, both glucose and FDG enter the glycolytic pathway and become phosphorylated. In the case of FDG however, the next step in the enzymatic process is halted since DG is not a substrate for glycolysis. In this way,  $^{18}\text{F}$ -labeled phosphorylated deoxyglucose is metabolically trapped within the cell, allowing for the PET imaging of trapped FDG in the tissue <sup>11</sup>. Acetate labeled with  $^{11}\text{C}$  is a commonly used tracer for tissue oxygen consumption since it is primarily metabolized by oxidative metabolism in the mitochondria. Unlike FDG being trapped in an enzymatic pathway,  $^{11}\text{C}$ -acetate is converted enzymatically to acetyl CoA and enters the citric acid cycle to produce adenosine triphosphate and is then cleared from the cell either in the form of  $^{11}\text{CO}_2$  or  $^{11}\text{C}$ -labeled amino acids. The clearance of  $^{11}\text{C}$ , therefore, gives an indirect measure of cellular oxygen consumption and can be used to identify normal or ischemic tissue <sup>4</sup>. All three of  $^{13}\text{N}$ -ammonia,  $^{82}\text{Rb}$  and  $^{15}\text{O}$ -water are blood flow or perfusion tracers and each have advantages and disadvantages. While the very short-lived  $^{82}\text{Rb}$  is a method of measuring perfusion without the need for costly cyclotron production, it produces images with lower spatial resolution due to its large positron range (Table 1.1), and requires larger correction for extraction from the blood when imaging quantitatively. Water labeled with  $^{15}\text{O}$  is considered the gold standard in PET perfusion measurements since it is freely diffusible across the capillary membrane and is extracted from the blood almost entirely in its first pass through the arterial blood. A

disadvantage of  $^{15}\text{O}$ -water includes its rapid decay resulting in low quality images due to the small number of coincident photons detected. Although an on-site cyclotron is required,  $^{13}\text{N}$ -ammonia is a well-established flow tracer used in the detection of coronary artery disease using PET. The following section describes in detail the characteristics of  $^{13}\text{N}$ -ammonia as a perfusion tracer and the methods used to extract quantitative physiological parameters of blood flow.

### 2.3 - The One Compartment Model

Compartmental modeling is the most common method to mathematically represent the physiological processes of uptake and clearance of tracer within a tissue<sup>11</sup>. In compartmental modeling, each compartment represents a state of the tracer, or more specifically in the case of  $^{13}\text{N}$ -ammonia among other tracers, the location of the tracer. Ammonia is freely diffusible across the capillary membrane and is highly extracted from the blood. Once extracted,  $^{13}\text{N}$ -ammonia crosses the cellular membrane and is metabolically trapped inside the cell in the form of  $^{13}\text{N}$ -glutamine. Because  $^{13}\text{N}$ -ammonia is highly extracted from the blood across the capillary membrane<sup>12</sup>, the influx constant  $K_1$  is a direct estimate of myocardial blood flow (MBF). Figure 2.1 illustrates the one compartment model that is used, at early time points, to estimate MBF by modeling the diffusion from the blood into a freely diffusible intercellular space, neglecting the slow metabolic trapping inside the cell.

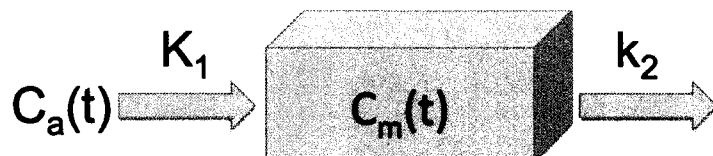


**Figure 2.1 A one compartment model used in perfusion quantification with  $^{13}\text{N}$ -ammonia**

Let  $C_a(t)$  represent the arterial blood radioactivity concentration and let  $C_m(t)$  denote the myocardial tissue radioactivity concentration. The rate constants  $K_1$  and  $k_2$  describe the influx and efflux respectively, into and out of the myocardial tissue. Although both  $K_1$  and  $k_2$  are rate constants, the units associated with them are not the same, indicated by the conventional capitalization of  $K_1$ . Typical radiotracer concentrations in blood are measured in activity per unit volume whereas radiotracer concentrations in tissue are measured in activity per unit mass. Since typical rate constants have units of  $\text{min}^{-1}$ ,  $K_1$  is forced to have units of  $\text{ml}/\text{min}/\text{g}$  in Equation 2.1.

In order to obtain temporal information regarding the blood and tissue concentrations, dynamic PET images are sampled both spatially and temporally to obtain accurate representations of radioactivity over time known as time activity curves (TAC). To obtain a blood time activity curve,  $C_a(t)$ , also known as an input function to the kinetic model, a small volume within the centre of the left ventricular cavity, away from the surrounding tissue is sampled. To obtain a tissue time activity curve,  $C_m(t)$ , the left ventricular myocardial tissue volume is sampled. This sampling is done semi-automatically using FlowQuant<sup>©</sup>, an in-house developed software suite to re-orient reconstructed images, sample the blood pool and myocardium temporally and apply kinetic modeling techniques for quantitative analysis.

The general differential equation describing the changing tissue concentration over time shown in Figure 2.1 is given by

$$\frac{dC_m(t)}{dt} = K_1 C_a(t) - k_2 C_m(t) \quad (2.1)$$

If at time = 0, there was an impulse function of activity in the blood, the corresponding solution would be given by

$$C_m(t) = K_1 e^{-k_2 t} \quad (2.2)$$

such that the tissue response would have an amplitude of  $K_1$ , and drop off exponentially over time described by  $k_2$  as illustrated in Figure 2.2.

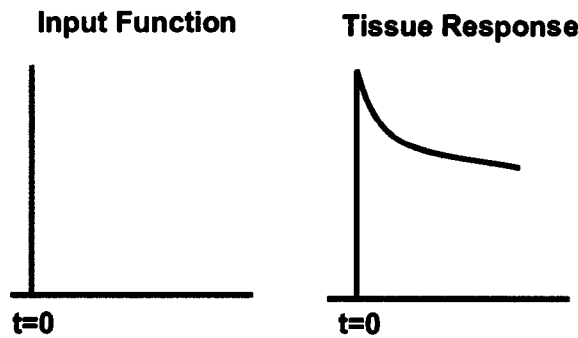


**Figure 2.2 Tissue response given an impulse input function at t=0**

In reality, the input function is not an impulse function, but rather a continuous function of activity over time. The situation illustrated in Figure 2.2 can then be extended to the continuous case in which any input function can be represented in terms of discrete impulses of varying amplitudes due to the linearity in  $C_a(t)$ . In response to the input, the summation of individual tissue responses can then constitute the tissue response function. This is, in general, the basis of convolution and it can be shown that the solution of Equation 2.1 for a continuous input is given by

$$C_m(t) = C_a(t) \otimes K_1 e^{-k_2 t} \quad (2.3)$$

where  $\otimes$  denotes a convolution operation. Ideal blood and tissue time activity curves for  $^{13}\text{N}$ -ammonia are shown in Figure 2.3 where the tissue curve is described by Equation 2.3 with arbitrary, fixed rate constants.

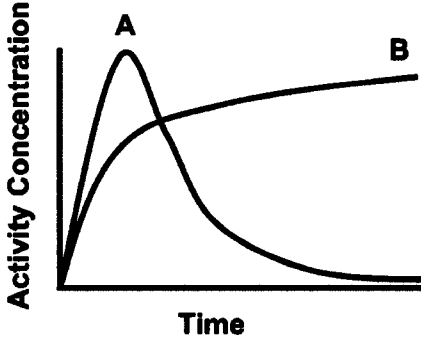


Figure 2.3 Ideal A) blood and B) tissue time activity curves for  $^{13}\text{N}$ -ammonia

One parameter that is used in the modeling process that is not defined in Figure 2.1 is the distribution volume (DV). Assume the flux into the tissue compartment is given by Equation 2.1 and the concentration of radioactivity in the blood,  $C_a(t)$ , remained constant (i.e.  $C_a(t) = C_a$ ). Eventually, an equilibrium would be reached and the net flux would equal 0. The DV is defined as the ratio of the tissue concentration to blood concentration at equilibrium, or more specifically,

$$DV = \frac{C_m}{C_a} = \frac{K_1}{k_2} \quad (2.4)$$

and can be thought of as the volume of blood that contains the same amount of activity as one gram of tissue<sup>11</sup>. The use of DV in parametric fitting will be discussed in later in the chapter.

Up to this point in this section, it has been shown that, according to Equation 2.3, the tissue time activity curve can be solved for analytically knowing the input function,  $C_a(t)$  and the model rate constants  $K_1$  and  $k_2$ . This, however, is not the objective of

quantitative tracer kinetic modeling. The objective is to accurately estimate the model rate constants given the measured blood time activity curve  $C_a(t)$  and the measured tissue time activity curve  $C_m(t)$ . To estimate the rate constants, a non-linear least squares method can be employed. Specifically, the goal in a least squares method is to minimize the sum of the squared differences between the measured tissue data and the predicted tissue data based on Equation 2.3 by iteratively varying the model rate constants<sup>11</sup>. Once the sum has been minimized, the rate constants can be identified including the value of quantitative myocardial perfusion,  $K_I$ , in units of ml/min/g.

In addition to the estimation of  $K_I$  and  $k_2$  by the method of least squares, there exists another equation incorporated into the model to account for partial volume losses and spillover of activity from the blood to the myocardium (See Chapter 3 for detailed explanation). This spillover is also known as total blood volume (TBV) and ranges in value from 0 to 1<sup>13</sup>. The model equation that includes TBV is given by

$$C_{pet}(t) = (1 - TBV)C_m(t) + TBVC_a(t) \quad (2.5)$$

which describes that the measured signal,  $C_{pet}(t)$ , which primarily originates from the tissue with some partial volume losses ( $1 - TBV$ ) but has some additional signal originating from the blood spillover into the tissue ( $TBV$ ).

In anticipation of large amounts of spillover in small rodent hearts and to account for spillover from the myocardium into the blood, an algebraic spillover correction method is presented in the Appendix.

Finally, by iteratively varying values of  $K_I$ ,  $k_2$  (or  $DV$ ) and  $TBV$  to minimize the sum of squares, accurate estimates of quantitative myocardial blood flow can be obtained, taking into account the blood spillover and partial volume losses.

The next section describes how this modeling process can be applied on a voxel-by-voxel basis in order to produce parametric images.

## 2.4 - Parametric Imaging

Parametric images are images that contain values obtained through tracer kinetic modeling rather than the conventional uptake images that display the radioactivity concentrations obtained from the PET camera. Parametric images can be obtained by performing tracer kinetic modeling on dynamic PET data on a voxel-by-voxel basis and displaying that value back inside that voxel.

A convenient method for displaying parametric images of the left ventricle of the heart is to use a polar map. A polar map is a two-dimensional representation of a three-dimensional, hemispherical left ventricle with the apex in the centre (AP) and the septal (SEP), lateral (LAT), anterior (ANT) and posterior (POST) walls as indicated in Figure 2.4.

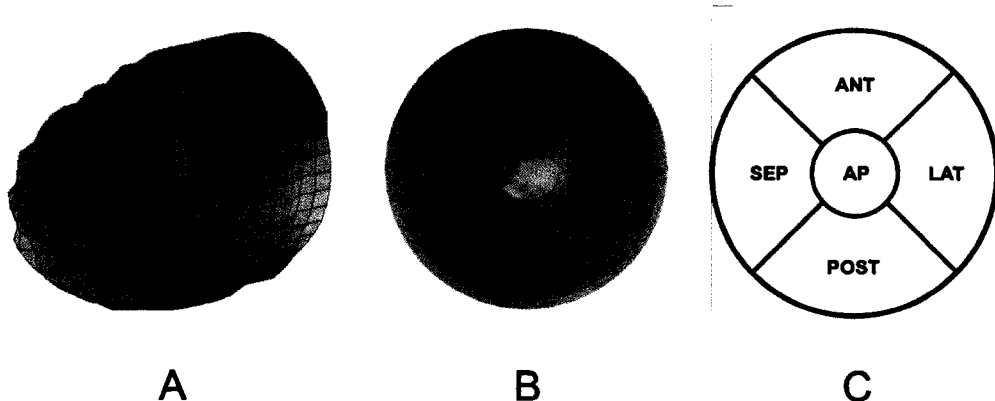


**Figure 2.4** A 3D left ventricle (A) can be represented as a 2D polar map (B) corresponding to anatomical segments (C)

In the one compartment model outlined in the previous section, parametric images of the left ventricle can include regional values of  $K_I$ ,  $DV$  and  $TBV$  as illustrated in the representative FlowQuant<sup>©</sup> output shown in Figure 2.5.

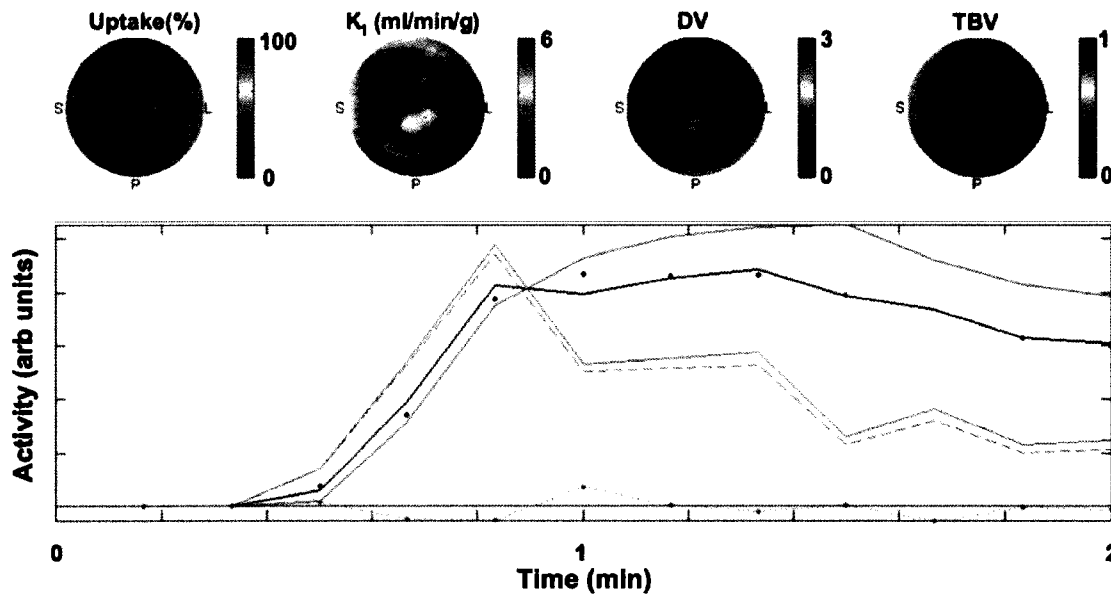


**Figure 2.5 Representative normalized uptake polar plot and parametric polar plots of  $K_I$ ,  $DV$  and  $TBV$  resulting from the kinetic modeling of  $^{13}\text{N}$ -ammonia rat data using FlowQuant<sup>©</sup> and the one compartment model described in the previous section. The bottom panel illustrates typical measured blood (red solid line) and tissue (blue data points) TACs along with the fitted tissue TAC (dark blue solid line), the residuals (green dashed line) and the predicted tissue TAC (light blue solid line)**

By displaying the fitted parameters in this way, functional processes can be described not only across the entire left ventricle, but also on a regional scale. In the case of PET perfusion imaging, polar plots of uptake and  $K_I$  are essential in the diagnosis, treatment and therapy tracking of single-vessel or multi-vessel disease.

## **Chapter 3 - Myocardial Perfusion Imaging: Current Advancements in Humans and Animals**

In order to provide motivation for the current study, Chapter 3 summarizes current research findings in the field of myocardial PET perfusion imaging with  $^{13}\text{N}$ -ammonia in humans. In addition to this, it outlines some of the recent work as well as some of the challenges associated with pre-clinical cardiac imaging in small animals. Before any current research is presented, a basic overview of the anatomy of the heart, coronary arteries and the standard reorientation of the heart is presented.

### **3.1 - Anatomy**

The heart consists of four chambers and four valves and works as two separate pumping systems. Initially, deoxygenated, venous blood empties into the right atrium from both the inferior and superior vena cava. The right atrium pumps the blood through the tricuspid valve into the right ventricle (RV) where it is further pumped through the pulmonary valve to the lungs via the pulmonary artery. Returning from the lungs, oxygenated blood empties into the left atrium where it is further pumped into the left ventricle (LV) through the mitral valve. In the final step, oxygenated arterial blood is pumped from the left ventricle through the aortic valve into the aorta where it is circulated through the body. Figure 3.1 illustrates this process schematically.

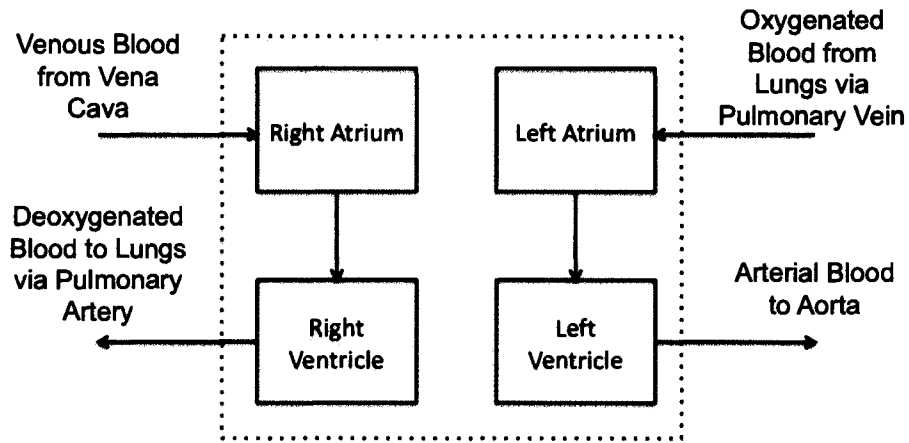


**Figure 3.1 A schematic diagram of the four chambers of the heart**

While the atria are pumping chambers, they act simply to pump venous and arterial blood to the ventricles which are the main pumps that provide the force that propels the blood into circulation. For this reason, there are large differences in the thickness in the atrial muscle tissue and the ventricular muscle tissue as well as in the physical size of the chambers. The thickest of the muscle tissues, the LV tissue is highly visible in PET images and is used to diagnose left ventricular dysfunction and coronary artery disease. Figure 3.2 is a typical slice of a rat heart through the ventricles showing clearly the LV and lower intensities originating from the RV.

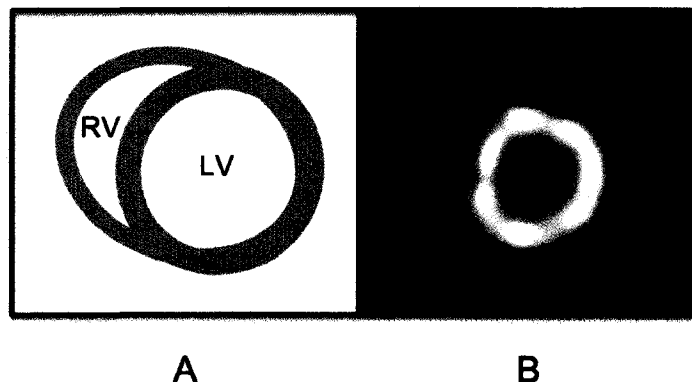


**Figure 3.2 A) A schematic drawing of a transaxial slice through the left and right ventricles of the heart. B) A typical transaxial view of a rat heart using  $^{13}\text{N}$ -ammonia**

Although it is convenient to step through image slices transaxially (i.e. along the axis of the body), the heart is situated at an angle with respect to the body's axis so transaxial slices do not clearly depict the ventricular chambers accurately. Conventionally, the image data is reoriented in such a way that the line from the apex to the mitral valve becomes orthogonal to the display with the LV and RV aligned horizontally<sup>14</sup>. Each reoriented image plane therefore depicts short axis (SA) views. From these SA views, orthogonal planes can be cut in vertical and horizontal directions as to show the vertical long axis (VLA) and the horizontal long axis (HLA) as shown in Figure 3.3.

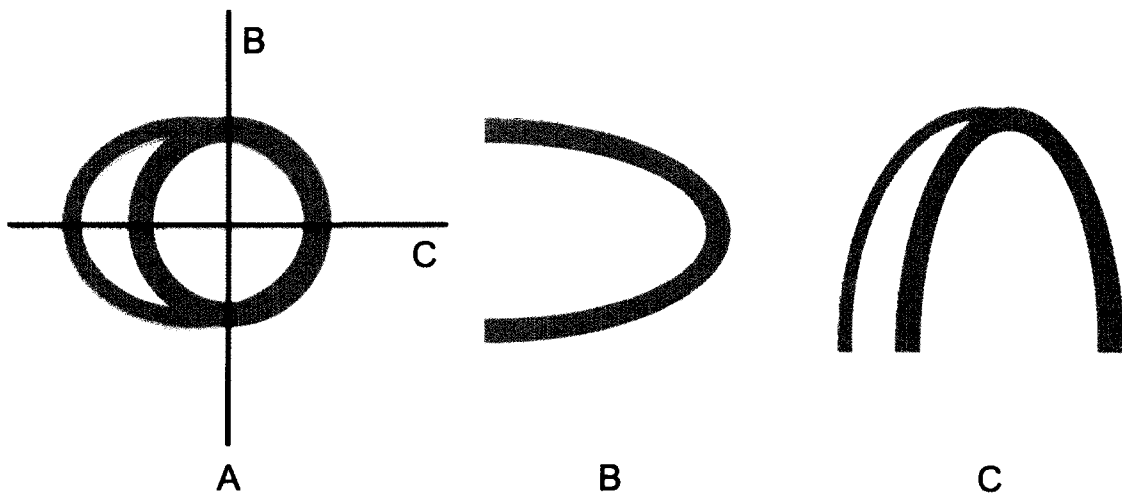


**Figure 3.3 Standard reorientation of the heart in PET imaging to clearly depict the LV. A) SA B) VLA C) HLA**

In order to accurately assess myocardial blood flow in the major coronary arteries, their location in relation to the tissue they supply needs to be known *a priori*. The right

coronary artery (RCA) supplies blood to some of the right ventricle in addition to the posterior wall of the left ventricle <sup>15</sup>. The left coronary artery branches into the left anterior descending (LAD) artery which supplies the apex and anteroseptal portion of the LV and the left circumflex (LCX) artery which supplies the lateral wall.

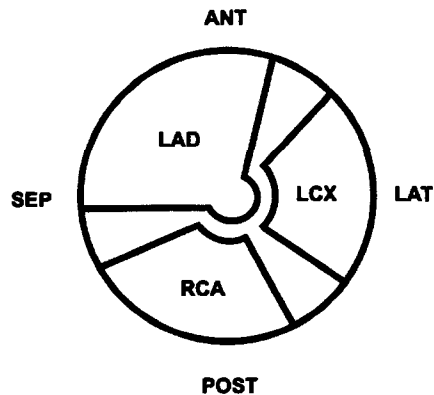


**Figure 3.4 Regions supplied by the coronary arteries as represented in polar map form**

In polar map display, the regions supplied by the main coronary arteries are shown in Figure 3.4 and will be pertinent in the discussion of detecting regional disease in myocardial blood flow measurements in rat myocardium with <sup>13</sup>N-ammonia in Chapter 7.

### **3.2 - Human Perfusion Imaging**

Both relative and absolute measurements of myocardial blood flow are established techniques in diagnosing coronary artery disease in humans. In relative perfusion imaging, tracer uptake in the tissue is normalized in the image so that any diseased area in the LV can be identified by a focal reduction in tracer uptake (See Figure 2.5). In absolute perfusion imaging, however, a quantitative scale is affixed to the images through parametric imaging so that absolute values of blood flow can be obtained. This

demonstrates population variability as well as the presence of multi-vessel disease, not possible with relative imaging.

In relative perfusion imaging, or tracer uptake imaging, reconstructed images of the heart acquired late after injection are displayed on a normalized scale (0-100% of maximum pixel intensity) either in polar map form or in SA, VLA and HLA slices. In both displays, perfusion defects are identified based on amount of tracer uptake and subsequently graded based on their severity according to their size and contrast relative to the surrounding normal tissue displayed at or near 100% uptake. This method of relative imaging is not limited to perfusion studies since it can be applied to most metabolically trapped tracers such as FDG. Uptake imaging using FDG is commonly used to qualitatively identify regions of the LV that have reduced glucose utilization. This, in conjunction with perfusion imaging is a commonly used protocol to assess myocardial viability and to predict the outcome in patients after surgical intervention. In a diseased heart, blood flow supplied by one or more coronary vessels could be reduced, however the tissue that it supplies may still be alive (viable). In this case, an MBF measurement using <sup>13</sup>N-ammonia would show reduced tracer uptake in the ischemic region while the FDG image would show normal tissue metabolism with no FDG uptake defects. This is termed a mismatch and would indicate that LV function as assessed by left ventricular ejection fraction (LVEF) would improve with surgical intervention. In contrast, an ischemic region of the LV that demonstrates a match, both <sup>13</sup>N-ammonia and FDG defects, indicates the presence of non-viable tissue and fibrosis predicting that LV function will not improve <sup>16-19</sup>.

Although uptake imaging has proved to be useful in the detection and prognosis of coronary artery disease, methods have been established and validated to quantitatively evaluate blood flow to allow for the absolute, regional comparison between normal and diseased cardiac tissue.

Using tracer kinetic models similar to the one compartment model described in Chapter 2, measurements of absolute perfusion in humans at rest in units of ml/min/g have been extensively studied over the past twenty years using both  $^{13}\text{N}$ -ammonia and  $^{15}\text{O}$ -water<sup>20-26</sup>. Limiting the discussion to only  $^{13}\text{N}$ -ammonia PET derived measurements of MBF, measurements from normal subjects range from 0.75 ml/min/g to 1.1 ml/min/g<sup>21-23;26</sup> but can include smaller or larger values. Evident from the large range of absolute values from multiple studies, there exists significant population variability. Within some human sample populations, resting absolute MBF values have variability as high as 57%<sup>26</sup> and as low as 15%<sup>27</sup>.

Absolute resting myocardial blood flow in humans has also been shown to increase with age<sup>22;28;29</sup>. This increase in flow has been attributed to increases in systolic blood pressure at older ages. Cardiac work can be estimated by the product of heart rate and systolic blood pressure, known as the rate pressure product (RPP) and correlates well with myocardial blood flow at rest<sup>22</sup>. In 1993, Czernin *et al.* obtained PET measurements of MBF in 40 normal volunteers in which they were divided into two groups. One group had a mean age of  $31 \pm 9$  years (n=18) and the second group had a mean age of  $64 \pm 9$  years (n=22). They showed a significant increase in absolute myocardial blood flow in the older group ( $0.92 \pm 0.25$  ml/min/g) versus the younger

group ( $0.76 \pm 0.17$  ml/min/g,  $p<0.05$ ) that was attributed to significant, measurable differences in the RPP between the groups.

Absolute MBF imaging in humans allows for the definition of normal MBF ranges, allowing for the detection of global reductions in perfusion and tracking of coronary artery disease on a quantitative scale. With the advancement of new instrumentation, small animal PET has developed into a powerful tool to non-invasively evaluate myocardial perfusion pre-clinically and response to its therapies *in vivo*.

### **3.3 - Rodent Perfusion Imaging**

More recently, with the advent of small animal PET scanners, pre-clinical investigations of myocardial perfusion in rats and mice have been carried out over the past five to ten years. Although, it has been shown that there are significant effects on absolute perfusion measurements with differing anaesthetic agents<sup>30;31</sup>, the majority of this data is concordant between studies. Two major imaging modalities are used to assess regional MBF values in rodents. Firstly, MRI has been used to investigate regional MBF using spin-labelling techniques on a pixel-by-pixel basis to form parametric short-axis images of the heart<sup>31-35</sup>. A second method for the determination of MBF in rodents, and the more pertinent to this discussion is with the use of small animal PET. Although the methods of tracer injection, dynamic data acquisition and tracer kinetic modeling are similar, the results of resting blood flow are very different from the human population. Typical resting flows for rats, as found by MRI, range from  $3.5 \pm 0.1$ (SEM) ml/min/g<sup>35</sup> to  $5.9 \pm 1.1$  ml/min/g<sup>33</sup> while <sup>13</sup>N-ammonia<sup>30</sup> and <sup>15</sup>O-water<sup>36</sup> PET studies have shown values of  $4.0 \pm 1.0$  ml/min/g and  $4.1 \pm 1.4$  ml/min/g respectively. Perfusion values in mice have been studied, but to a lesser extent due to the technological difficulties in

manufacturing small animal PET systems with adequate resolution and producing doses of high enough concentrations<sup>37</sup>. Mouse MBF values seem to be slightly higher than rat values but very susceptible to differences not only in the type of anaesthetic, but its concentration<sup>31;38</sup>. Kober *et al.* studied perfusion values at rest in mice using MRI and found an MBF of  $6.9 \pm 1.7$  ml/min/g at an isoflurane concentration of 1.25%. With the concentration of isoflurane increased only to 2%, the MBF value increased to  $16.9 \pm 1.8$  ml/min/g with no difference in heart rate<sup>31</sup>. This study indicates that mouse MBF is extremely sensitive to levels of anaesthetic and must be carefully controlled in comparative studies.

The major difficulties involved with myocardial imaging in rats and mice are motion artifacts attributed to the beating heart and respiration. In addition to motion, the small physical dimensions of the heart also make myocardial imaging in small animals challenging. Most small animal scanners have gating capabilities in order to eliminate most of the motion blur due to respiration and the cardiac cycle. In a study by Yeng *et al.*<sup>31;39</sup> however, it was concluded that although cardiac gating greatly improved image quality in mouse studies, respiratory gating did not significantly improve the results. To overcome the difficulty of imaging small rodent hearts, the system's spatial resolution is critical and will improve primarily through advances in detector technology and reconstruction algorithms. The rat LV internal diameter measures approximately 5-6 mm with a wall thickness of approximately 2 mm<sup>40;41</sup>. When fully relaxed (end-diastole), the wall thins even further<sup>40</sup>, pushing the resolution limits of most scanners. When imaging a structure with less than two times the system resolution, partial volume effects appear to underestimate the radioactivity present in the small tissue. Consider a short axis view of

a cardiac rat phantom with dimensions as shown in Figure 3.5A. Due to finite resolution, the myocardial tissue in the reconstructed image is blurred by the point spread function of the system, extending the activity outside the boundaries of the tissue and effectively lowering the peak activity. This underestimation of activity is shown in the line profile across the LV in Figure 3.5B. The recovery coefficient (RC) can be defined as a parameter between 0 and 1 that relates the peak activity measured to the true activity present ( $\text{Observed } C_m / \text{True } C_m$ ). Tissue radioactivity registered in the blood pool is known as spillover from the tissue to the blood. Similarly, the activity in the blood pool is blurred into the myocardial tissue space as shown in Figure 3.5C and is known as spillover from the blood into the tissue. This spillover of signal contributes to the vascular fraction of blood inside the tissue region or TBV as discussed in Chapter 2 and RC can be represented as  $1 - \text{TBV}$ .

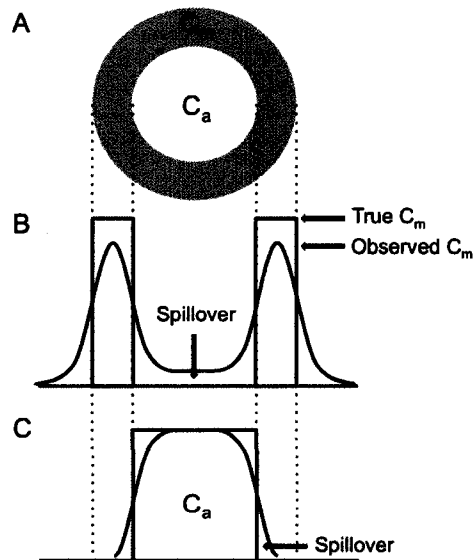


**Figure 3.5 A)** Illustration of a short axis view of a cardiac rat phantom with the corresponding line profile of measured radioactivity signal across the LV originating from the B) myocardium and C) blood pool indicating spillover into each

These partial volume and spillover effects are incorporated into the kinetic model as discussed in the previous chapter to obtain more accurate measurements of MBF.

The purpose of this chapter was to provide motivation for the current study as it outlined some of the major findings of PET perfusion imaging in humans as well as in small animals. In addition to method development and the successful translation of clinical image analysis techniques to small animals, this work extends the current knowledge base of myocardial blood flow in normal rats. It establishes a population variability, a database of normal absolute MBF values similar to published values, investigates the test-retest reproducibility of these measurements and, for the first time, reports an age-related increase in baseline myocardial blood flow in rats. Chapters 5, 6 and 7 outline, in detail, the methodology and results from the current study and discuss the importance of these findings in future investigations evaluating myocardial blood flow non-invasively, serially and *in vivo*.

## **Chapter 4 - Siemens Inveon™ PET Scanner Performance Specifications**

In order to achieve usable, high quality images in small laboratory animals such as rats and mice, high sensitivity and high resolution is of utmost importance. One of the leading small animal PET systems currently on the commercial market is the Siemens Inveon™ PET scanner. Some of the features that make it one of the leading small animal imaging systems are high resolution, large axial field of view and high sensitivity.

Very different in size from a clinical PET scanner, the Inveon's detector ring is only 16.1 cm in diameter with a bore size of 12.0 cm. The camera also has a large axial field of view of 12.7 cm making it possible to easily image an entire mouse body and almost image an entire rat without using the continuous bed motion feature. This continuous bed motion feature allows for the subject to be passed through the detector ring while data acquisition is taking place, extending the effective axial field of view to 50 cm. Inside the detector ring are packed 64 detector blocks each consisting of a 20 x 20 array of 1.5 mm x 1.5 mm x 10 mm lutetium oxyorthosilicate (LSO) elements resulting in 25,600 highly-packed, optically isolated LSO elements coupled to position-sensitive photomultiplier tubes.

LSO is a scintillation material and has advantageous properties for PET imaging. It is a very dense material allowing for high linear attenuation at 511 keV and therefore capable of stopping and detecting large numbers of photons that impinge on its surface. It also has high light output of approximately 13,000 photons for each incident 511 keV photon, important in the accurate determination of where the scintillation event or energy deposition took place. Finally, LSO has fast decay time of approximately 47 ns which is

crucial for the timing resolution of the imaging system and how fast it can recover to detect another incident photon. Table 4.1 lists the properties of some commonly used scintillation materials for photon detection at 511 keV.

**Table 4.1 Properties of scintillation materials commonly used in PET detectors<sup>6</sup>**

Scintillation Material	Density (g/cc)	Light Output (photons/incident)	Decay Time (ns)	$\mu_{\text{tot}} @ 511 \text{ keV} (\text{cm}^{-1})$
Sodium Iodide [NaI(Tl)]	3.67	19400	230	0.34
Bismuth Germanate (BGO)	7.13	4200	300	0.96
Lutetium Oxyorthosilicate (LSO:Ce)	7.40	~13000	~47	0.88
Gadolinium Oxyorthosilicate (GSO:Ce)	6.71	~4600	~56	0.70
Barium Fluoride (BaF <sub>2</sub> )	4.89	700, 4900	0.6, 630	0.45

In addition to the detector size and material, the Inveon™ camera has unmatched performance specifications in spatial resolution, count rate and sensitivity. The system is capable of generating reconstructed images with  $\leq 1.4$  mm full width at half maximum (FWHM) resolution using FBP and is capable of even higher resolutions using the fully three dimensional iterative reconstructions available in the software suite. In terms of count rate, this system's peak noise equivalent count rate (NEC), which gives a global measure of signal to noise, is quoted to be 2.0 Mcps which is the highest among all other small animal PET imaging systems. To compare this value, other small animal imaging systems such as the LabPET4, microPET-F120, and the quad-HIDAC have peak NEC values of 42 kcps, 809 kcps and 45 kcps respectively<sup>42</sup>. The system sensitivity defined

as the counting efficiency for a known activity, is also unmatched among small animal PET cameras. The sensitivity of the Inveon™ has been quoted to have  $\geq 10\%$  sensitivity while the LabPET4, microPET-F120, and the quad-HIDAC have sensitivities of 0.6%, 7.1% and 1.2% respectively. This high sensitivity allows for the injection of very low tracer amounts due to low tracer concentrations and reduces the need for large amounts of cyclotron-produced radioactivity. Using low amounts of injected tracer using a PET system with high sensitivity, can still result in statistically high quality reconstructed images.

To complement the system's notable performance characteristics, it has many capabilities to customize various imaging protocols and post-processing techniques. The Inveon™ has the capability to perform transmission imaging for the purposes attenuation correction. Inside a shielded gantry around the bore of the scanner is housed a  $^{57}\text{Co}$  source used for transmission imaging. The source is rotated around the subject such that attenuation can be measured. In conjunction with a blank scan (no object in the FOV), attenuation correction factors can be obtained as discussed previously in Chapter 1 to be used in image reconstruction. Cobalt-57 emits photons at a much lower energy of 122 keV in contrast to the photons typically detected at 511 keV. Linear attenuation coefficients vary both in material as well as photon energy. In using a lower energy, there is more contrast seen in the transmission images between bone and soft tissue since the difference in linear attenuation coefficients is greater at 122 keV. Although the transmission source is in place, the system has the capability to incorporate CT-derived attenuation maps into the image reconstruction given adequate image co-registration. The advantage of using CT for attenuation correction is that it provides a more

anatomically accurate representation of the subject with minimal noise. This almost noise-free CT image will not propagate as much noise into the reconstructed image as would a  $^{57}\text{Co}$ , PET derived transmission image.

This small animal PET scanner acquires data in list-mode format allowing for use of physiological gating. In gating studies, the subject's cardiac and/or respiratory cycles are monitored and TTL logic pulses are sent from the physiological monitoring device at specified times within the cycle. These signals are then recorded by the PET system and incorporated into the list-mode data file. When rebinning this data, it is possible to synchronize the acquired data with the cardiac or respiratory cycle to obtain images at different times within the cycle. Gating greatly reduces blur caused by cardiac and respiratory motion and therefore increases the resolution of the acquired images. The disadvantage of gating is that by dividing the image into time bins, it will reduce the statistical quality of the reconstructed images due to lower count densities. The Siemens Inveon™ system not only has the capability for dual cardiac and respiratory gating in tandem, it can also acquire dynamic gated images, extracting time activity curves from specific gates within the cardiac or respiratory cycle.

Finally, in order to operate with high throughput, the system needs to be stable without the quality of the acquired images degrading over time. To assess this stability, a daily quality assurance (DQC) protocol is in place in order to track the system's performance over time and to identify any anomalies if they arise. To perform a DQC, a cylindrical  $^{68}\text{Ge}$  flood phantom with a radius 3.0 cm was centred in the FOV and the DQC factory pre-set acquisition was started. The results from this DQC included the mean counts across all detector blocks as well as the system's timing resolution. These

parameters were recorded on a daily basis to give a metric of the daily system performance. The manufacturer quoted that maintenance would be required if the system's mean counts per detector block divided by the standard deviation (SD) falls below 3.5 or if the timing resolution becomes greater than 1.5 ns. Figures 4.1 and 4.2 are data collected in the first five months after installation indicating the system's stability over time.

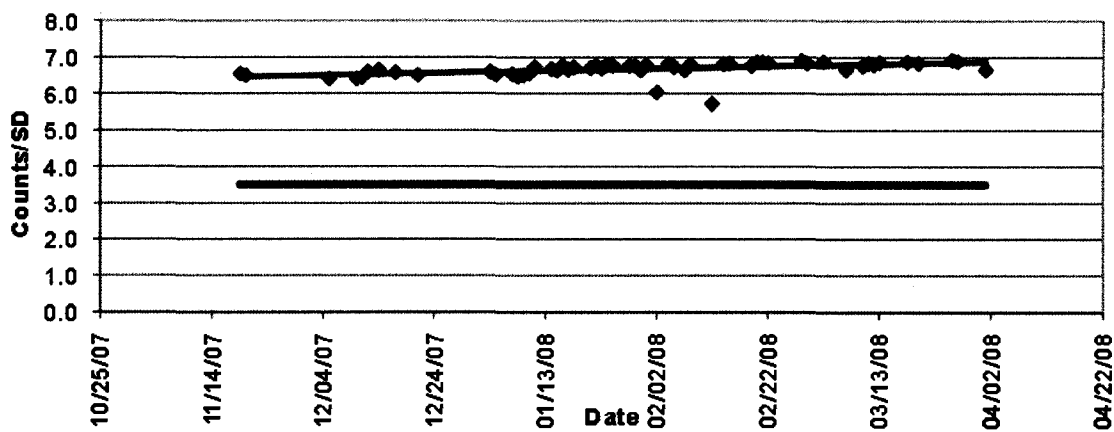


**Figure 4.1 Counts/SD for the first five months after installation. Values below the solid red line indicate the need for maintenance**

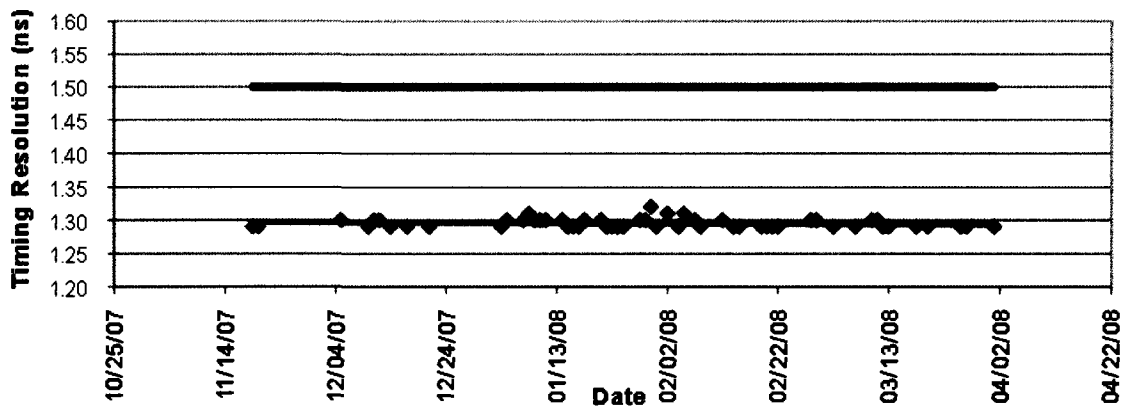


**Figure 4.2 System timing resolution for the first five months after installation. Values above the solid red line indicate the need for maintenance**

Evident from Figures 4.1 and 4.2, the PET system is extremely stable over time and performing well above the manufacturer's quoted specifications for maintenance. The origin of the linearly increasing trend in the counts/SD plot (Figure 4.1) is still unknown, however, it was noted by the manufacturer that in the first few months, the system was operating at a very high temperature possibly keeping it from performing optimally. This temperature was just below the critical shutdown temperature and required a new piece of hardware to cool the scanner back down to normal ranges. Further to this, the room in which the scanner is situated had become increasingly colder since the start of 2008 possibly cooling the machine down closer to the optimal operating temperature.

The Siemens Inveon™ small animal PET scanner has been shown and quoted to be a cutting-edge imaging system capable of providing high resolution dynamic PET images of small animals. The subsequent chapters will describe in detail the methods

used and the results obtained in developing non-invasive, *in-vivo* protocols for the accurate and reproducible measurements of MBF in normal and diseased animals.

## **Chapter 5 - Qualitative and Quantitative Imaging of Rat Myocardial Blood Flow with $^{13}\text{N}$ -ammonia**

### **5.1 - Imaging Protocol and Analysis Methods**

Non-invasive small animal PET imaging was carried out on the Siemens Inveon™ scanner. Male Sprague Dawley rats (Charles River, Canada) were anaesthetized by placing them in an induction box for 5-10 min using 2% isoflurane. Once anaesthetized, they were transferred to the preparation area where they lay supine with a nose cone delivering constant isoflurane. Ocular lubricating gel was applied to the eyes to maintain lubrication throughout the procedure and to prevent the formation of cataracts. A tail vein catheter was inserted into one of the two tail veins. The tail vein catheter was capped and taped to the rat's tail for easy intravenous (IV) injection of radiotracer. The rat was then transferred to the scanner bed laying supine with a nose cone placed over the nose of the rat to ensure steady isoflurane anaesthetic for the duration of the scan. A bed heater was maintained at 34°C or 36°C to help maintain body temperature. A pressure-sensitive respiration monitor was placed between the animal and the scanner bed, or was taped to the animal's chest to provide constant monitoring of the animal's respiration rate. Two subcutaneous electrocardiogram (ECG) leads were placed bilaterally under each forelimb. A separate lead was placed subcutaneously in the groin region. The ECG signal was used to monitor the heart rate of the animal and was also connected to the scanner in order to gate the cardiac signal into the list-mode data file for later processing. The animal was positioned both vertically and horizontally using the onboard laser positioning system, so that the heart was centered in the FOV of the

scanner. Once the animal was centered in the FOV, the radiotracer activity was measured using a dose calibrator (Capintec) and the time was recorded to the nearest second. The scanner was started 5-20 sec prior to radiotracer injection in order to capture the entire input function. A bolus injection of approximately 75-110 MBq (2-3 mCi) of  $^{13}\text{N}$ -ammonia in 1.0 ml was injected intravenously over a 5-10 second period. Following the injection, approximately 100-200  $\mu\text{l}$  of 0.9% saline was injected to flush the catheter of any remaining activity. List-mode data was acquired for 30 min using a 350-650 keV energy window and a timing window of 3.432 ns. After the scan, the rat was weighed, put back in its cage, and kept behind shielding until all remaining radioactivity had decayed. Dynamic PET data was rebinned into 20 frames of varying lengths. The first twelve frames were 10 seconds, the next three frames were 60 seconds and the final five frames were 300 seconds. This dynamic framing is also used clinically and provides adequate sampling to generate TACs. After the dynamic data was rebinned, it was reconstructed using the OSEM3D/MAP iterative algorithm with corrections for detector efficiencies, randoms and with the parameters shown in Table 5.1. Attenuation and scatter correction were not incorporated into the reconstructions.

**Table 5.1 Selected reconstruction parameters used in generating rat perfusion images**

Field	Value
Image Matrix Size	128x128
Zoom	2.5
OSEM Iterations	2
MAP Iterations	18
Resolution (mm)	1.0
Uniform	Variance
FastMAP	ENABLED

The OSEM and MAP iterations are the manufacturer's suggested default and the resolution value of 1.0 mm imposes a small smoothing kernel. FastMAP is a Siemens-

specific option used in a MAP algorithm optimized for speed. Using the parameters shown in Table 5.1, the resulting 128x128 reconstructed images had an x and y pixel dimension of 0.34 mm and a transaxial (z) image plane spacing of 0.80 mm. Figure 5.1 shows representative reconstructed images of a rat heart using  $^{13}\text{N}$ -ammonia.

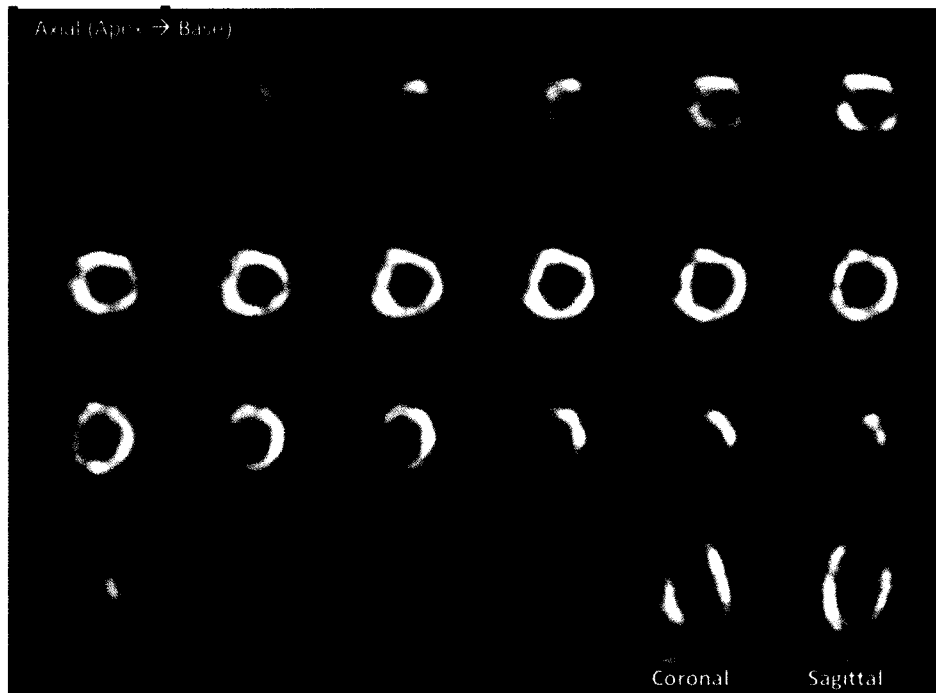


**Figure 5.1** A representative reconstructed image of a rat heart using  $^{13}\text{N}$ -ammonia showing axial slices from the apex (top left) to the base (bottom middle). Coronal and sagittal views are also shown

From the reconstructed images, analysis was performed using in-house developed FlowQuant<sup>®</sup> software. This software semi-automatically sampled the myocardial tissue and blood pool both spatially and temporally in order to obtain TACs. From these TACs, tracer kinetic modeling was performed resulting in parametric polar maps. Relative uptake polar maps (%) were generated using the last 28 min of the scan and absolute MBF polar maps (ml/min/g) were generated from the first 2 min of data. Significant changes were made to the processing parameters in order to successfully translate the

clinical processing software to small animals. The processing parameters used in the analysis of the reconstructed images are tabulated in Table 5.2. The radial sampling parameters refer to the thickness of the sampling volume across the LV wall. Smoothing parameters also exist such as kernel size and uptake resolution which smooth the dynamic and uptake data respectively. The start and end times refer to the time limits used in the tracer kinetic modeling.

**Table 5.2 Processing parameters used in the analysis and modeling of rat perfusion images**

Field	Value
Radial Sample Endo (mm)	0.5
Radial Sample Epi (mm)	0.5
Kernel Size (mm)	1.5
Uptake Frames	8
Uptake Resolution (mm)	2.0
Normal Uptake Threshold (%)	75
Start Time (min)	0
End Time (min)	2

The one compartment DV model discussed in Chapter 2 was used to generate parametric polar maps of MBF (ml/min/g), DV and TBV in addition to standard uptake polar maps on a relative scale (%). Each parametric polar map was divided into 18 rings of 36 sectors in order to produce 648 estimates of regional blood flow. The median  $K_1$  (MBF) value in the polar map was taken to be the global value of MBF. To investigate segmental measurements of MBF as shown in Figure 2.4C, the polar map was divided into 5 segments corresponding to the apical, septal, lateral, posterior and anterior segments of the LV. All data presented are mean  $\pm$  SD unless otherwise stated.

## 5.2 - Optimization of Blood Pool Sampling Volume

Some processing parameters needed to be adjusted before any image analysis could proceed using software written for clinical PET images. One of these parameters

was the blood pool sampling volume. This volume is defined by the radius of a cylinder used to sample the centre of the LV cavity when viewed on its short axis. This cylinder is also divided into three equal regions corresponding to the cavity, the base and the atrium; the locations closest to which it samples. A typical human heart has a left ventricular chamber diameter of approximately 55 mm and a wall thickness of 10 mm<sup>43</sup>. In humans, the sampling radius used in FlowQuant<sup>®</sup> is 6.0 mm. A typical rat heart, however, can be approximated to have a left ventricular chamber diameter of 5-6 mm and a wall thickness of only 2 mm<sup>40;41</sup>. In a simple scaling down of sampling radii from chamber diameters, the rat's sampling radius should be in the range of 0.65 mm.

To investigate the sampling radius, its value was varied using values of 3.0, 1.5, 0.75 and 0.50 mm using a high-quality dynamic FDG rat image. An FDG image was used due to its high count statistics and the ease it provides in accurately determining the edges of the myocardium. Figure 5.2 shows the TACs resulting from the four different sampling radii. The tissue TAC is shown as the solid blue line whereas the blood median TAC (median of the cylinder containing regions sampled close to the cavity, base and atrium) is shown to be the solid, dotted red line.

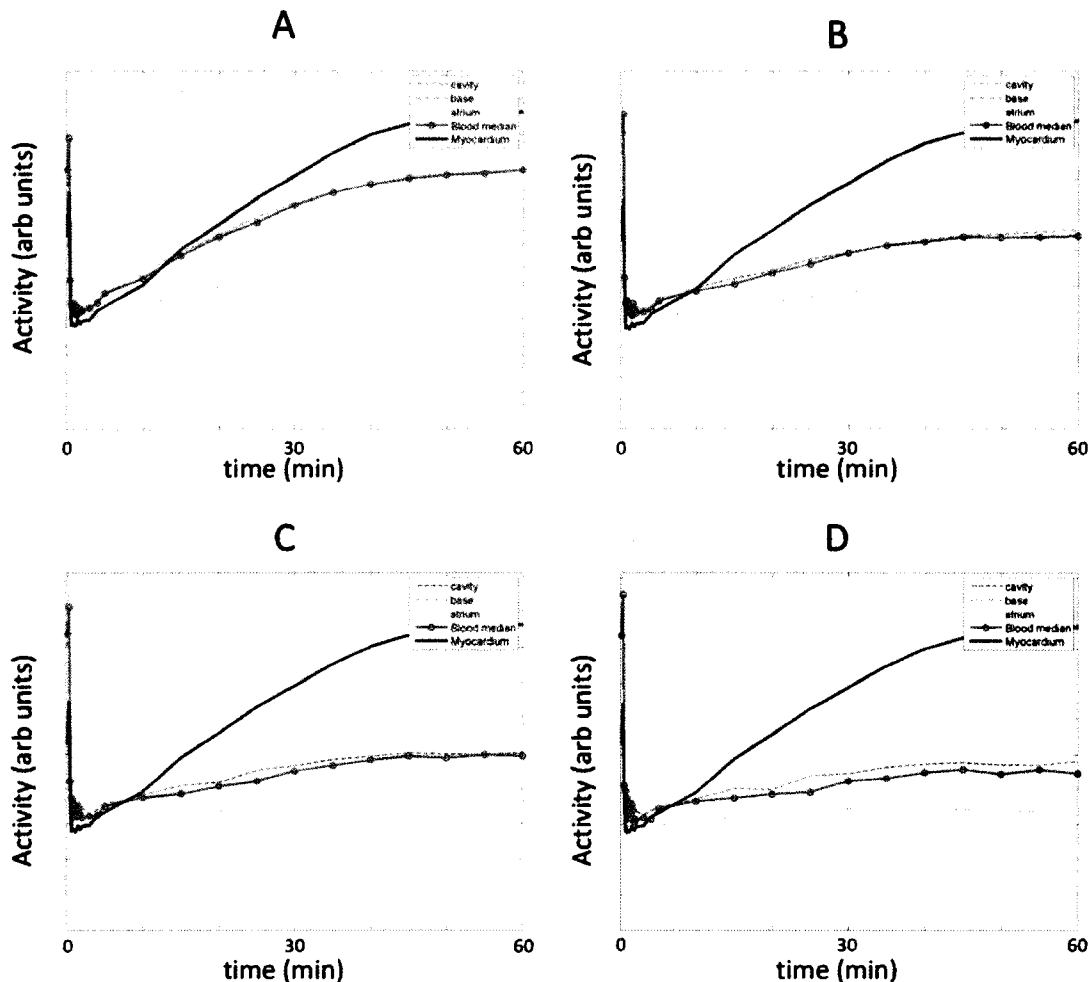


**Figure 5.2 Time activity curves resulting from four different sampling radii of A) 3.0 mm B) 1.50 mm  
C) 0.75 mm D) 0.50mm**

Although the tissue activity (blue solid line) should not have changed between the four analyses, slight variations in the TAC exist due to the four independent tissue samples required to array the blood cavity sampling radius. The ideal FDG blood TAC should decrease to zero over time since the FDG is being taken up from the blood. Comparing the blood time activity curves in panels A-D of Figure 5.2, it is evident that panel A has the most significant amount of spillover, or misregistration of tissue activity in the blood. It is clear that the sampling radius is too large at 3.0 mm as it has the highest amount of

spillover and is likely sampling some of the myocardial activity. As the sampling radius gets smaller (Figure 5.2A-D), the spillover from the tissue into the blood decreases as less correlation between the curve is observed. However, as the sampling radius becomes smallest at 0.50 mm (Figure 5.2D), noise in the blood curve starts to become apparent due to the Poisson nature of detected events in the reconstructed image. Also evident in Figure 5.2 is the atrial blood curve (light green curve below blood median), originating from the atrial compartment of the sampling cylinder. This TAC exhibits less spillover than the other two blood curves (cavity and base) with similar noise properties as the median curve. This illustrates that the atrial blood curve has the potential to be used as a more accurate input function for these studies. Panels A-D in Figure 5.2 also show a spike in radioactivity in the tissue curve indicative of spillover from the blood into the myocardium.

The least amount of spillover from the tissue into the blood and a minimally noisy blood curve are required for a true representation of the blood TAC. A sampling radius of 0.75 mm was chosen as this was shown to have the least amount of spillover into the blood curve without significant noise. Further justifying the choice of 0.75 mm was the theoretical hypothesis of 0.65 mm as approximated by a simple scaling down of the human sampling radius. Shown in Figure 5.3 are VLA and HLA slices of a representative normal rat heart with the corresponding, appropriately adjusted sampling volume shown inside the cavity.



**Figure 5.3 VLA and HLA slices of a normal rat heart after automatic reorientation showing the appropriately adjusted blood pool sampling volume in the cavity (C), base (B) and atrium (A). The solid line indicates the tissue region sampled. The circles on the tissue are handles for user intervention**

Once the blood pool sampling volume had been optimized and other processing parameters had been scaled down to produce accurate blood and tissue TACs, absolute quantitative MBF measurements in rats were achievable.

### **5.3 - Relative and Absolute MBF Population Variability**

One of the objectives of this work was to develop and validate PET imaging methods for accurate and reproducible relative and quantitative measurements of perfusion in rodent models of heart disease and to evaluate the population variability that exists within these normal samples. To accomplish this, a total of 21 animals were scanned according to the methods described in Section 5.1 and both relative uptake (%) and MBF (ml/min/g) polar maps were generated. Polar maps for the first six subjects are shown in Figure 5.4 to illustrate both the variability between subjects as well as the

difference in polar map uniformity from relative uptake (top row) to absolute MBF (bottom row).

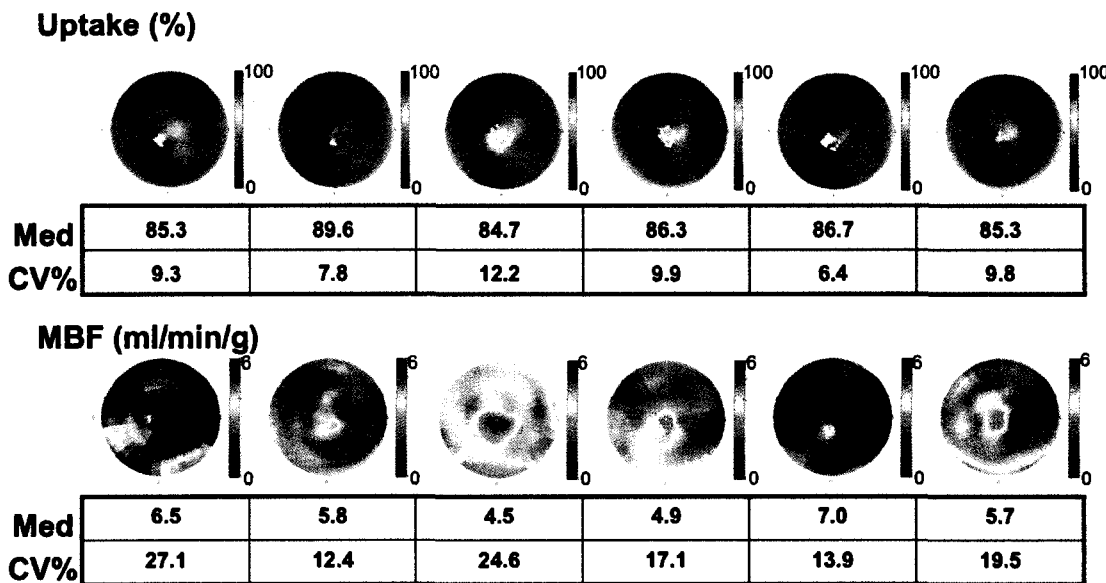


**Figure 5.4 Individual polar maps of relative (0-100%, top row) and absolute (0-6 ml/min/g, bottom row) perfusion in the first six subjects to illustrate the variability between subjects and the uniformity in each polar map. Med=median, CV=coefficient of variation**

In some of the uptake polar maps, it is evident that there are sectors missing near the apex. This is due to user intervention at the re-orientation stage of the software where the user can crop out any non-cardiac tissue from the image volume. In the case of ammonia, it is highly taken up in the liver which is situated just below the heart and therefore interferes with the myocardial signal. It is typical to crop the liver activity and small portions of the apical region of the heart in order to preserve the myocardial signal originating from the rest of the LV. In the kinetic modeling stage of the software, these missing regions are filled in and approximated by interpolation from the surrounding sectors. Also shown in Figure 5.4 are median LV values and coefficient of variations (CV) across each polar map. The LV median is used to describe the 648 sectors in the

polar map since median values are not influenced by occasional outlying sector values.

The CV is defined as the ratio between the standard deviation and the mean and will be used to assess polar map uniformity. Consequently, a low CV value indicates a uniform polar map. It is assumed and expected that from a normal, heart disease-free sample population of animals, myocardial perfusion should be uniform across the entire ventricle. Therefore, good uniformity as assessed by small CV values is a measure of regional accuracy. From Figure 5.4, the relative uptake across the entire LV is quite uniform having CV values all less than 13% and a very narrow range of LV median values. Looking at the corresponding absolute MBF polar maps, the pattern of lower flow in the apical regions remains the same, however, the inhomogeneities in each polar map increase. This increase in CV in the MBF polar maps is a product of the tracer kinetic modeling process and/or a shorter time interval having less counts and therefore introducing noise into the final parametric image. This phenomenon of losing uniformity when using an absolute scale can also be seen in Figure 5.5 where uptake and MBF polar maps over the entire 21 subject population have been averaged on a sector-by-sector basis.

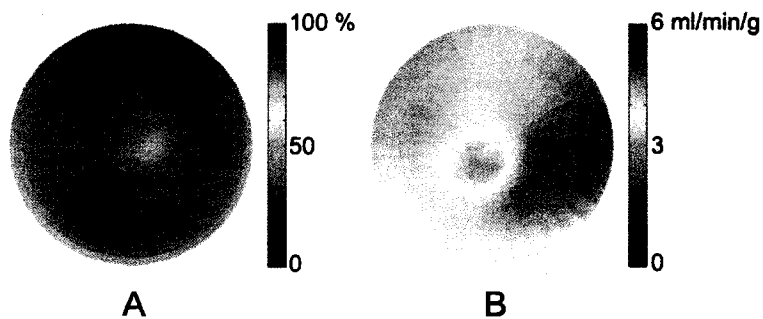


**Figure 5.5 A) Mean uptake and B) mean MBF polar maps across the sampled population (n=21)**

Table 5.3 summarizes the relative and absolute LV medians, corresponding population variabilities and CV values collected from the 21 normal subjects.

**Table 5.3 Summary statistics (mean  $\pm$  SD) of LV relative and absolute perfusion values with corresponding CV measurements (n=21)**

	<b>LV Median</b>	<b>Population Variability (%)</b>	<b>CV (%)</b>
<b>Uptake</b>	$85.3 \pm 3.7\%$	4.3	$8.6 \pm 1.7$
<b>MBF</b>	$4.3 \pm 1.1$ (ml/min/g)	26.5	$16.8 \pm 4.7$

Concordant with the first six subjects (Figure 5.4), the uptake median values of the sample population have a very narrow distribution of  $85.3 \pm 3.7\%$  which represents only a 4% population variability. The uptake polar maps are also quite uniform with a mean CV value of  $8.6 \pm 1.7\%$  consistent with the assumption that these normal rats do not have any coronary artery disease that negatively affects perfusion in the LV. Moving from the relative scale to the absolute scale, the polar maps become much more heterogeneous with a population CV value of  $16.8 \pm 4.7\%$ . The advantage of using MBF imaging, however, is to obtain an absolute physiologic measure of blood flow in ml/min/g. From this sample, the mean LV MBF value was  $4.3 \pm 1.1$  ml/min/g. This measurement is similar to previously reported rat MBF values as measured by MRI ( $3.5 \pm 0.1$ (SEM) ml/min/g<sup>35</sup> and  $5.9 \pm 1.1$  ml/min/g<sup>33</sup>), by <sup>13</sup>N-ammonia PET ( $4.0 \pm 1.0$  ml/min/g<sup>30</sup>) and by <sup>15</sup>O-water PET ( $4.1 \pm 1.4$  ml/min/g<sup>36</sup>). Although these image derived values, including the value obtained in this study, are precise, the accuracy still remains somewhat controversial. Microsphere studies have reported MBF values in rats at rest to be in the range of 5.0-9.0 ml/min/g<sup>44,45</sup>. Microsphere studies are invasive, terminal procedures, in which  $\mu$ m-sized radiolabeled polystyrene spheres are injected into the

bloodstream and lodge in the capillaries in proportion to blood flow. The microsphere procedure will be explained in detail in Chapter 6.

The population variability in absolute MBF in this normal sample was found to be 27%. Although seemingly high, this variability is consistent with previously published measurements of 19%<sup>33</sup>, 25%<sup>30</sup> and 34 %<sup>36</sup> using MRI, <sup>13</sup>N-ammonia PET and <sup>15</sup>O-water PET respectively. Even when compared to population variability in humans, this rat variability matches previously reported human values ranging from 57%<sup>26</sup> to as low as 15%<sup>27</sup>.

Methods for global, quantitative measurements of perfusion and population variability have been developed and have been shown to coincide with previously reported values. The next section will describe the methodology and results obtained when investigating perfusion measurements using a regional five segment model.

#### **5.4 - Relative and Absolute MBF Segmental Variability**

In addition to global MBF measurements, another objective of this work was to investigate the regional variability in both relative uptake and MBF polar maps, especially after the observation of the regional non-uniformities apparent in Figure 5.5. To do this, the sectors in the polar maps were divided into five segments representing the apical, septal, lateral, posterior and anterior portions of the LV. Representative segments are shown on the average uptake and average MBF polar maps as shown in Figure 5.6A-B. The mean  $\pm$  SD values in each segment of Figure 5.6C-D represent the population mean  $\pm$  SD across all 21 subjects in that segment. Comparing regions on each polar map, it is still evident that the uptake map exhibits a very narrow distribution of relative uptake, whereas the MBF values have larger variability in individual segments.

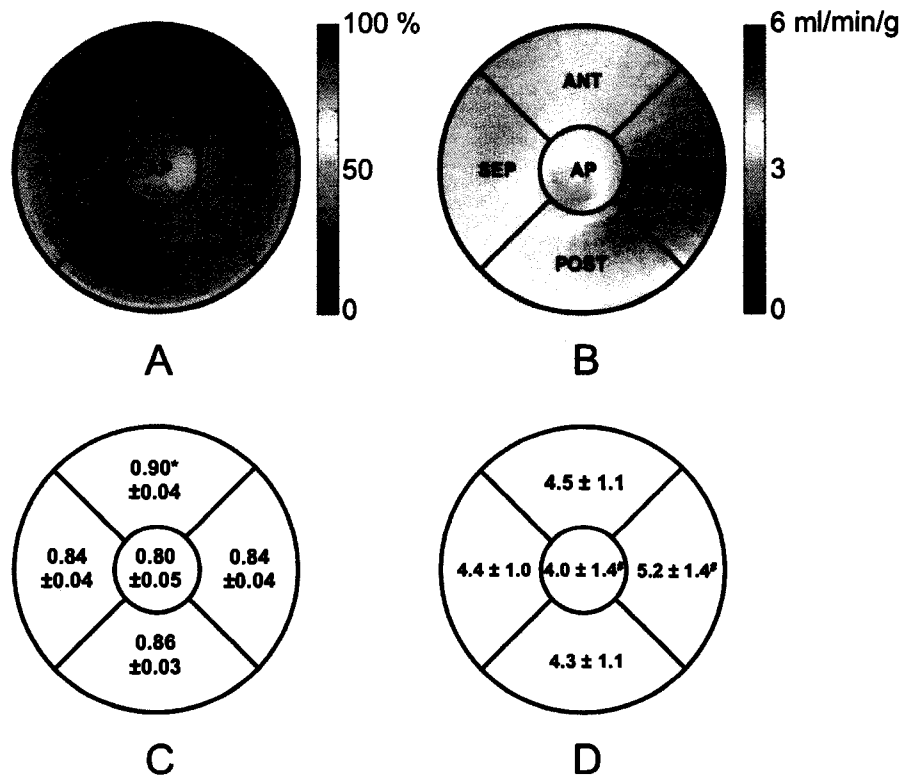


**Figure 5.6 A)** Mean uptake and **B)** mean MBF polar maps across the sampled population ( $n=21$ ) divided into five segments (apical, lateral, anterior, septal and posterior). Segmental statistics across the population are shown for **C)** uptake and **D)** MBF. \* denotes a difference between all other segments and # denotes a difference between the two segments ( $p<0.05$ )

The largest variability in both the uptake and MBF measurements is found to be in the apical region. The reduced uptake and MBF in the apex is a normal artifact in cardiac imaging possibly due to the thinner apical walls and reduced motion during the cardiac cycle. Also, a contributing factor to the higher variability in the apex in this study could be missing sector values in some polar maps originating from the cropping of interfering liver activity as discussed in Section 5.3.

In the uptake polar map shown in Figure 5.6C, the anterior region was shown to have a 5 % increase in uptake relative to all other segments ( $p<0.05$ ) denoted by \* and as measured by a one-way analysis of variance (ANOVA) and a subsequent multiple

comparison between regions. This increase in uptake is likely due to the absence of a transmission image used for attenuation correction at the time of image reconstruction. The reason for not using attenuation correction was purely logistical as the cobalt-57 transmission source had not been installed throughout the duration of this study. Anatomically, the anterior region of the heart is the closest to the surface of the body. As discussed in Chapter 1, less photon attenuation occurs and therefore more counts are registered when the radioactivity is located near the tissue surface. It is speculated that with correct incorporation of attenuation correction factors in the reconstructed images, this apparent increase in relative perfusion in the anterior region could be reduced or eliminated. Also, it is hypothesized that the relative uptake polar maps could be even more uniform with the use of proper attenuation correction techniques as measured by CV.

In Figure 5.6D, the lateral region was shown to have a 30% increase in absolute MBF as compared with the apex ( $p<0.05$ ) denoted by # and as measured by a one-way ANOVA and a subsequent multiple comparison between regions. Note that due to the large variability within each segment, only the apex and lateral wall are statistically different. Although this reduction of MBF in the apex is a known imaging artifact, the source of this apparent increase of MBF in the lateral wall is still unknown. It can be hypothesized that since this increase of tissue activity is not apparent in the uptake polar maps, it may be a systematic error in the kinetic modeling process. If there was a small bias in overestimating the TBV value on the lateral wall, possibly due to increased wall motion, this would drive the parametric fit of  $K_1$  to overestimate the actual MBF value in that region. The TBV polar maps suggest that there is no regional increase in TBV in the

lateral wall relative to the other segments and therefore the parametric fit of TBV is not likely the cause of the regional increase in MBF. Further investigations into the cause of this increase in MBF are required. Although, a perfusion increase in the lateral wall was observed relative to the known reduction of MBF in the apex, it is important to note that there were no significant differences compared to the other three segments, indicating similar regional variability across the normal sample population as to the global population variability quoted in Section 5.3.

### **5.5 - Perfusion Increase with Weight**

In order to obtain an accurate sample population, rats with diverse ages and masses were chosen for this study. After birth, a rat's mass increases quickly and continues to rise through its life-cycle<sup>46</sup>. A rat's age and weight are therefore positively correlated. In this study, perfusion measurements were performed on rats as young as 9 wks and as old as 14 wks with masses ranging from 248 g to 636 g respectively. An observed correlation between MBF and animal mass (and indirectly age) existed as is shown in Figure 5.7. This correlation has never been reported in rats.

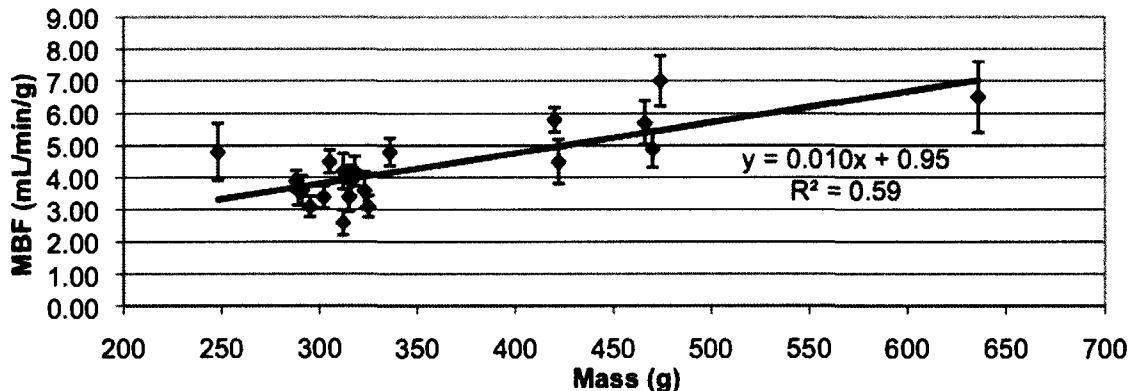


**Figure 5.7 MBF increase with weight. Errors on the MBF values are derived from the SD between the five segments within each polar map**

Errors on the LV median MBF values shown in Figure 5.7 and 5.8 are derived from the SD between the five segments within each polar map. A linear model was fit to the data with a coefficient of determination,  $R^2=0.587$ . Using a one-tailed t-test, this increase in MBF with mass was deemed to be significant ( $p<0.001$ ). A linear model was fit to the data to compare the linearity in MBF shown to be present in humans<sup>16</sup>. Although an increase in resting MBF in humans has been shown to be age-dependent<sup>22,28,29</sup>, it remains unclear whether the increase shown in rats in this study is age- or weight-related. In humans, the regression equation between age and resting MBFs is  $MBF=0.56 + 0.005\text{years}^{16}$ . Evident from Figures 5.7 and 5.8, the regression equation between mass and resting MBF is  $MBF=0.95 + 0.010\text{g}$  and between age and MBF is  $MBF=-2.58 + 0.673\text{wks}$ .

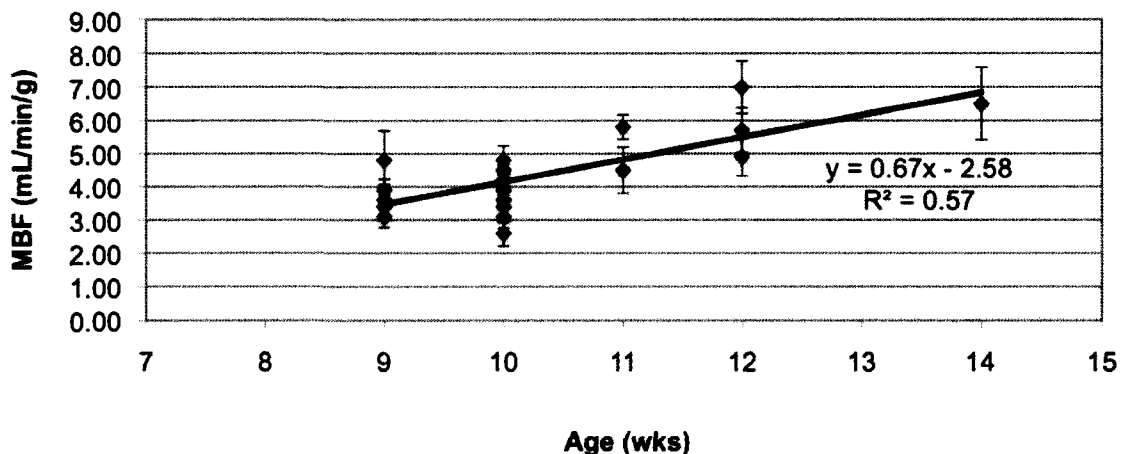


**Figure 5.8 MBF increase with age. Errors on the MBF values are derived from the SD between the five segments within each polar map**

Although this perfusion increase is consistent with previously reported human data, efforts were made to verify that this significant rise in resting rat MBF was not the result of a systematic error in the imaging method or in the analysis protocols. One factor that was investigated was the lack of attenuation correction used in reconstructing the final images. As discussed previously, radioactivity located deeper within tissue will register fewer counts in the final image than activity located near the surface of the tissue. If it is assumed that the radioactivity in the LV blood pool of a larger heart will undergo more attenuation than in a smaller heart, both relative to the myocardial tissue, it would systematically drive the fitted  $K_I$  value higher in the larger hearts. If it is assumed that the LV cavity in a large heart is 6.5 mm in diameter and the wall thickness is 2.5 mm<sup>41</sup>, then the centre of the cavity to the middle of the tissue would measure 4.5 mm. In a smaller heart, assume that the LV cavity is 5.0 mm in diameter having a wall thickness of 1.5 mm<sup>41</sup>, measuring 3.25 mm from the centre of the cavity to the middle of the tissue. Using this approximation, the 511 keV photons originating from positron decay in the LV cavity of

larger hearts would have to travel through an additional 1.25 mm of matter as compared to the smaller hearts. A simple calculation using the linear attenuation coefficient of water at 500 keV of  $0.0969 \text{ cm}^{-1}$ <sup>8</sup> reveals relative attenuation difference of approximately 1%. This insignificant amount of attenuation of the activity in the blood pool in larger hearts as compared to smaller hearts would not be enough to drive the MBF measurements as high as what was observed in Figures 5.7 and 5.8 and therefore can be discounted as a systematic imaging error.

Another source of error that needed to be addressed pertained to the model fitting of the TBV value. As mentioned in Chapter 2, incorporated in the one compartment model is a correction for a fraction of the blood activity being registered in the tissue region (TBV) as well as a correction for RC. It was hypothesized that the estimation of the RC value in the model fitting had a systematic influence on the outcome of the MBF measurements. The estimated RC values directly affect the model fitting of  $K_I$  since RC is used to compensate for signal recovery of small tissue thicknesses. Although there was a trend towards estimated RC values increasing with weight as shown in Figure 5.9, there was no correlation ( $p=0.12$ ), suggesting that the hearts in this sample population were not considerably different in size. More importantly, the resulting MBF measurement was not correlated to the estimated RC as shown in Figure 5.10 ( $p=0.29$ ), discounting the hypothesis that the estimated RC values systematically influenced MBF. In both Figures 5.9 and 5.10, the errors on the LV median MBF are derived from the SD between the five segments within each polar map, RC is estimated parametrically and the error on the mass is  $\pm 1\text{g}$ .

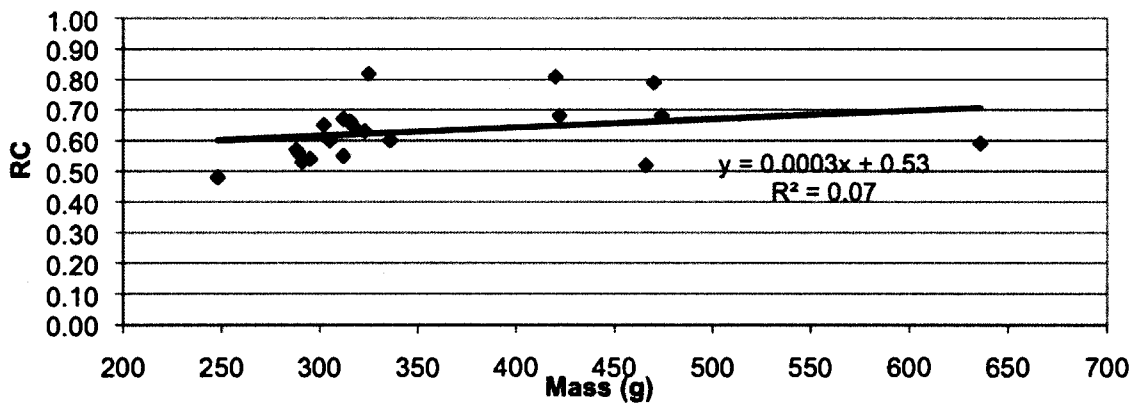


Figure 5.9 Estimated RC versus Mass (g)

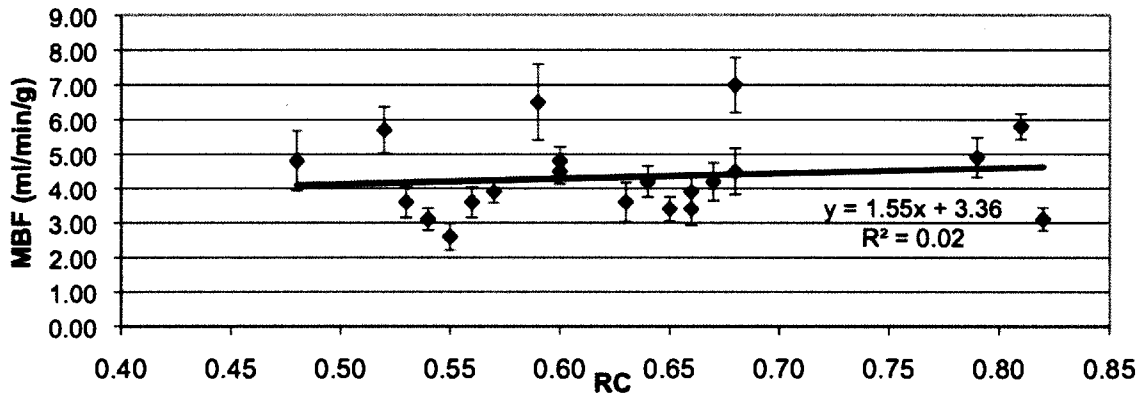


Figure 5.10 MBF versus estimated RC. Errors on the MBF values are derived from the SD between the five segments within each polar map

As stated previously, this age- or weight-related increase in MBF has never before been reported in rats. This data also suggests that this relationship can account for some of the apparent trends in MBF values found in the literature. Using MRI, Iltis and colleagues<sup>33</sup> measured MBF values in Wistar rats having masses of  $351 \pm 30$  g to be 5.9 ml/min/g whereas Waller *et al.*<sup>35</sup> report a lower MRI-derived value of 3.5 ml/min/g in smaller Wistar rats (250-330 g).

A known limitation in this investigation is the lack of documented heart rates and blood pressures for the 21 normal subjects. As mentioned in Chapter 3, the rate pressure product as measured by the product of heart rate and systolic blood pressure correlates well with myocardial blood flow in humans at rest<sup>22</sup>. Measurements in rate and pressure could have been used to validate the MBF values obtained in this study to illustrate the increase of MBF over the life cycle of the animal.

In all cases previously reported in rats, the quoted MBF values fall within the mean  $\pm$  SD found in this study. In light of this knowledge of an age- or weight-related increase in MBF, the population variability of 27% quoted in Section 5.3 over a rat population ranging in masses of 248 g to 636 g was considered an overestimation. By using a large subset ( $n=15$ ) of animals without a large range in mass ( $245 \text{ g} < m < 400 \text{ g}$ ), a new, more representative population variability was determined for this study. The population variability for animals of similar weight ( $245 \text{ g} < m < 400 \text{ g}$ ) was calculated to be 17%.

The importance of this newly reported increase in MBF over time not only affects the current knowledge of rat physiology, but has implications in the practical field of myocardial perfusion imaging to track and evaluate perfusion therapies. It is essential to take this relationship into consideration when comparing perfusion values obtained serially over the duration of an investigation. Another relevant requirement for the establishment of normal perfusion measurements is to detect significant, absolute changes between groups of animals in the presence of population variability and small sample sizes. The subsequent section describes and illustrates the usefulness of a

population variability measurement in a case study comparing two possible pre-clinical treatment groups evaluating myocardial perfusion.

### **5.6 - Case Study: Detecting Perfusion Changes in the Presence of Population Variability**

To illustrate the usefulness of a study of absolute perfusion measurements and their variability, the differences in weight and age presented in the previous section will serve as an example to detect perfusion changes in the presence of population variability. Two groups were created that differed significantly in age and weight (Table 5.4), however, the strain, imaging protocol, and analysis method remained identical.

**Table 5.4 Demographics of Groups 1 and 2**

	<b>Group 1 (n=6)</b>	<b>Group 2 (n=15)</b>
<b>Strain</b>	Sprague Dawley	Sprague Dawley
<b>Age (wks)</b>	$11.0 \pm 1.1^*$	$8.0 \pm 0.4^*$
<b>Mass (g)</b>	$481.3 \pm 79.5^{\#}$	$305.0 \pm 21.2^{\#}$

\* and # denote differences between groups (p<0.01)

The larger, older rats in Group 1 exhibited a mean  $\pm$  SD MBF of  $5.73 \pm 0.94$  ml/min/g.

The smaller, younger rats in Group 2 exhibited a mean  $\pm$  SD MBF of  $3.90 \pm 0.90$  ml/min/g indicating a reduction of 32% (p<0.01) as shown in Figure 5.11.

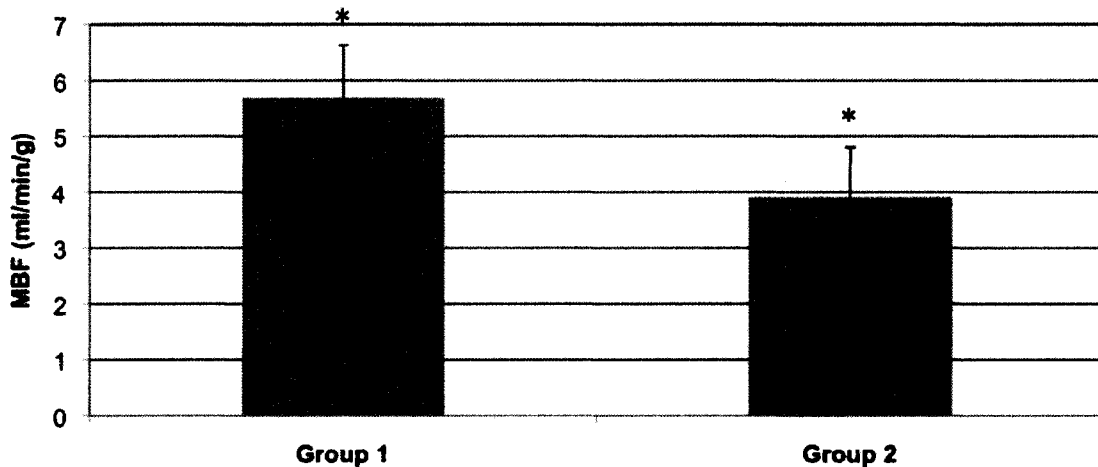


**Figure 5.11 Absolute MBF of Group 1 and Group 2. \*** denotes  $p<0.01$ . Error bars represent Group 1 and Group 2 SD

These two MBF values represent population variabilities of 17% and 23% for Group 1 and Group 2 respectively.

By establishing a database of normal MBF values and their variabilities, it is possible to perform sample size calculations. These calculations can predict acceptable sample sizes to ensure statistically significant differences between experimental treatment groups if they exist. For example, knowing that the mean MBF value of Group 2 is  $3.90 \pm 0.90$  ml/min/g, it is possible to predict the sample size necessary to detect a change equal to the SD (i.e. 23%). Using a two-sided test at a 95% confidence interval and a statistical power of 80%, a sample size of 16 animals would be required. Similarly, to detect a change equal to twice the SD (i.e. 46%), a sample size of only 4 animals would be required. In this case study, a significant 32% change was demonstrated using only 6 animals in Group 1.

In developing experimental protocols either by serially tracking myocardial perfusion over time or by comparing absolute perfusion between groups, sample sizes

and variability in normal data need to be addressed accordingly prior to making statistical inferences. In an effort to investigate other sources of variability in the measured data, the next section addresses the reproducibility of these measurements.

### **5.7 - Test-Retest Reproducibility**

As small animal PET imaging has become a powerful tool in quantitative and repetitive studies in rodents, another objective of this study was to quantitatively evaluate the test-retest reproducibility of this imaging method.

A subset of 9 normal rats were chosen out of the 21 normal subjects and subsequently re-scanned 3 days following their first scan for a total of 18 images. The imaging protocol and analysis method as outlined in Section 5.1 was followed. Bland-Altman plots<sup>47</sup> were used to demonstrate the difference between repeated measurements by plotting the test-retest difference between the two measurements versus their mean. The Bland-Altman plot of the test-retest repeatability is shown in Figure 5.12 where the red solid line indicates the mean difference, the grey dashed line indicates a zero difference, and the green dotted lines indicate the mean  $\pm$  2SD.

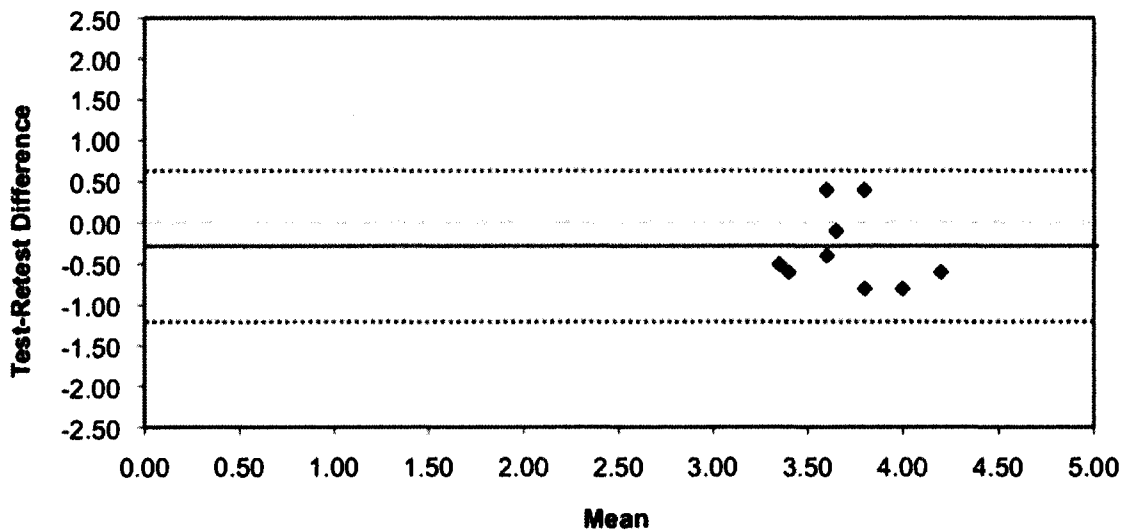


**Figure 5.12 Bland-Altman plot of test-retest reproducibility (n=9)**

From Figure 5.12, it is apparent that there is excellent reproducibility in MBF measurements as no differences are greater than 1.0 ml/min/g. The standard deviation of the differences was found to be 0.47 ml/min/g and the coefficient of repeatability (CR), defined as 2SD was calculated to be 0.94 ml/min/g or 25.3% of the mean MBF. To compare this CR value to published values, Chareonthaitawee *et al.* investigated the repeatability of  $^{13}\text{N}$ -ammonia PET measurements of MBF in pigs<sup>48</sup> and found a CR value of 26.6% of the mean MBF, quoting it as excellent. In humans, Nagamachi *et al.* reported that  $^{13}\text{N}$ -ammonia PET measurements of MBF are reproducible with a CR value of 31.6%<sup>49</sup>.

Also evident in Figure 5.12 is the systematic bias towards a negative difference, indicating greater values in the second measurement of MBF ( $p=0.06$ ). The mean difference was calculated to be -0.33 ml/min/g with only 2/9 measurements lying above the zero difference line. Although this systematic difference has not yet been identified,

one possible explanation is again due to the increase in MBF with weight. At the time of this study, the rats were fairly young and were growing rapidly at a rate of approximately 60 g/wk. Specifically, the second scan was performed 3 days post initial scan when the rats had shown a mean mass increase of  $22.3 \pm 4.2$  g. Using the linear MBF equation derived in Section 5.5 of  $\text{MBF} = 0.95 + 0.010g$ , a 22 g increase in weight could account for 0.22 ml/min/g of the apparent systematic bias seen in Figure 5.12. To investigate this bias further, same-day repeat measurements should be taken in accordance with animal care guidelines controlling for the effects of prolonged anaesthesia that have been documented in some cases<sup>30;33</sup>.

To conclude, the measurements have been shown to have a repeatability coefficient of 25.3% of the mean difference, consistent with previous reports of ammonia PET measurements of MBF in pigs and humans. There appears to be a systematic bias towards higher global MBF values in the second measurement which is consistent with the previously described correlation between MBF and weight. Further investigation into this bias is required using same-day protocols and more subjects.

## 5.8 - Intra-observer Repeatability

Another source of variability in MBF measurements in rats is intra-observer variability. After the data has been acquired and the images have been reconstructed, the kinetic modeling steps have some user intervention steps subject to variability. Specifically, when the software is orienting the LV from transaxial, coronal and sagittal planes to SA, VLA and HLA planes as discussed in Chapter 3, the user usually needs to manually fit a partial ellipsoid to the LV in the image volume as well as crop out any

interfering liver activity. The objective of this experiment was to quantify the intra-observer repeatability associated with this method.

The same subset of 9 normal rats (18 images) was chosen out of the 21 normal subjects as in the test-retest method. These 18 images were re-processed by the same observer as in Section 5.7. The analysis methods and settings outlined in Section 5.1 were used. A Bland-Altman plot was used to demonstrate the difference between repeated measurements by plotting the difference between the two measurements versus their mean. The Bland-Altman plot of the intra-observer repeatability is shown in Figure 5.13 where the red solid line indicates the mean difference, the grey dashed line indicates a zero difference and the green dotted lines indicate the mean  $\pm 2SD$ . Note that some data points overlap due to the same difference and mean.

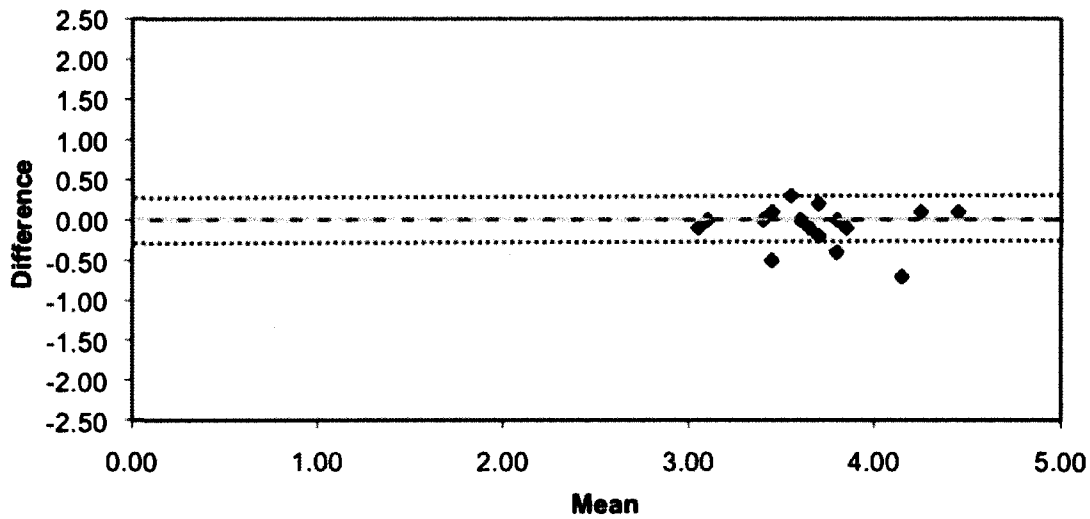


**Figure 5.13 Bland-Altman plot of intra-observer repeatability (n=18)**

The intra-observer repeatability was excellent. The SD of the differences was found to be 0.16 ml/min/g and the CR was calculated to be 0.32 ml/min/g or 8.2% of the mean MBF which is well below the population variability and test-retest variability. Also shown in Figure 5.13 is the lack of systematic bias. The mean difference was calculated to be 0.03 ml/min/g with eight measurements lying above the zero difference line, six below it, and four on it.

### **5.9 - Inter-observer Repeatability**

Finally, an experiment was conducted to quantify the inter-observer variability of MBF measurements resulting from variability associated with some user intervention steps in the re-orientation stage of the software.

The same subset of 9 normal rats (18 images) was chosen out of the 21 normal subjects as in the test-retest method. These 18 images were re-processed by a different observer as in Section 5.7. The analysis method and settings outlined in Section 5.1 were used. A Bland-Altman plot was used to demonstrate the difference between repeated measurements by plotting the difference between the two measurements versus their mean. The Bland-Altman plot of the inter-observer repeatability is shown in Figure 5.14 where the red solid line indicates the mean difference, the grey dashed line indicates a zero difference and the green dotted lines indicate the mean  $\pm$  2SD. Note that some data points overlap due to the same difference and mean.

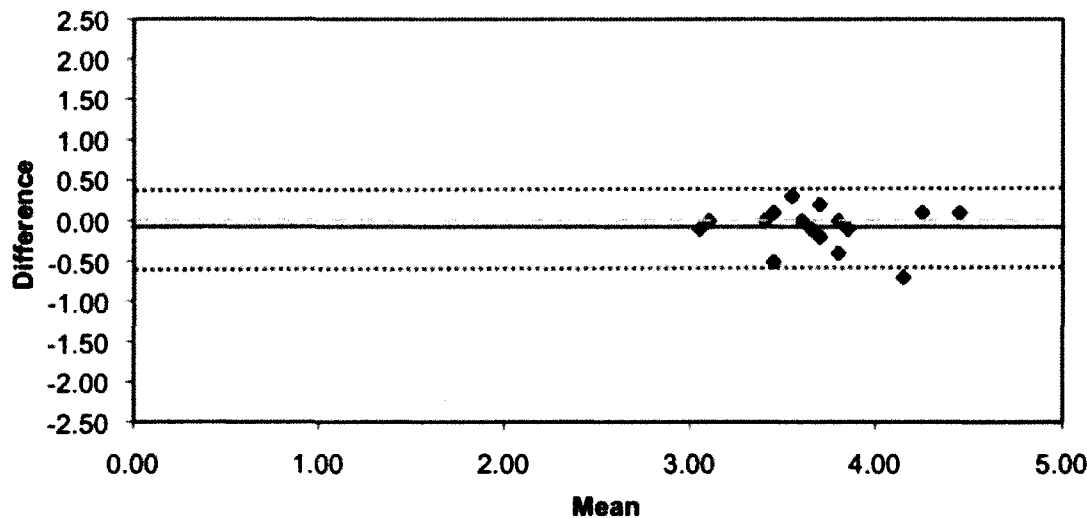


**Figure 5.14 Bland-Altman plot of inter-observer repeatability (n=18)**

The inter-observer repeatability was excellent, but as expected, was more variable as compared to the intra-observer repeatability. The SD of the differences was 0.25 ml/min/g and the CR was calculated to be 0.50 ml/min/g or 13.2% of the mean MBF. Although more variable than the intra-observer repeatability, this inter-observer variability is still below the population variability and test-retest repeatability. Evident from Figure 5.14, there is the lack of systematic bias with points equally scattered around the zero difference line. The mean difference was calculated to be -0.07 ml/min/g with six measurements lying above the zero difference line, seven below it and six on it.

## 5.10 - Conclusion

Results to date have shown that although the uptake polar maps showed excellent uniformity consistent with a normal population and small population variability of 4%,

the absolute MBF measurements affixed a quantitative, physiological scale to these measurements. The MBF population variability over the entire 21 subjects was found to be 26.5%, a value in agreement with previously reported population variability of MBF in rats. These previously published results derived from MRI, <sup>13</sup>N-ammonia PET and <sup>15</sup>O-water PET also gave consistent global MBF values to the value of  $4.3 \pm 1.1$  ml/min/g obtained in this study.

Regionally across the LV, differences were observed between the anterior segment and all other segments in the uptake map as well as between the lateral and apical segments in the MBF polar map. The slightly higher uptake in the anterior segment was most likely due to the lack of correction for attenuation in the final, reconstructed image. The increase in MBF in the lateral wall, however, cannot be explained as easily. Since this increase was not apparent in the uptake image, the origin of this bias may be from the tracer kinetic modeling stage. It should be noted, however, that the apex is known to have a decreased MBF, and no significant difference in MBF was observed between the lateral segment versus the anterior, posterior or septal segments. Further experiments to investigate the increased measured MBF in the lateral wall need to be conducted.

Secondly, a new finding was presented revealing an age- or weight-related increase of myocardial perfusion in rats at rest. This increase was modeled as a linear effect in light of previously published reports of linear, age-related increases of myocardial perfusion at rest in humans. In an effort to further investigate this correlation and discount any systematic imaging or analysis errors, both the lack of attenuation correction and biased estimates of RC in hearts of different sizes were thoroughly

studied. These effects were shown to have no bearing on the MBF measurements and therefore this correlation of MBF with age or weight was taken to be a real, observed effect. With this new information, the population variability of 27% presented in Section 5.3 was considered an overestimation. A new, revised population variability was quoted to be 17% taking a subset of 15 subjects with small variability in mass.

In Section 5.6, a case study was presented using the current data in order to illustrate the need for established, absolute MBF measurements with their corresponding population variabilities. These measurements are essential for quantitative, statistical comparisons between groups and to calculate sample sizes needed in an experimental design evaluating myocardial perfusion.

In the final three sections of this chapter, data was presented quantifying the test-retest reproducibility, the intra-observer repeatability, and the inter-observer repeatability. The test-retest reproducibility of the imaging and subsequent analysis methods proved to have excellent reproducibility having a CR value of 25.3% of the mean MBF. This is consistent with published values of reproducibility using  $^{13}\text{N}$ -ammonia PET measurements of MBF in pigs and humans. The test-retest data, however, shows a systematic bias towards measuring increased MBF 3 days after the initial scan. It has been hypothesized that this bias would become less apparent when the 20-30 g discrepancy of each animal between scans was taken into account using the linear model described in Section 5.5. The intra-observer variability was found to be small having a CR of 8.2%. As expected, the inter-observer variability was slightly larger at 13.2%. Both variabilities were found to be small compared to the population variability indicating that the analysis protocols are robust and negligibly biased by human

intervention. The data, however, suggests a small advantage of single-operator processing.

Although these absolute perfusion measurements have been compared to numerous published findings and were shown to be precise, validation of these measurements was necessary in order to assess their physiological accuracy in the normal rat heart. To investigate the accuracy of the MBF measurements, the next chapter describes more invasive experiments conducted using radiolabeled microspheres which are considered to be the gold standard for validating flow measurements.

## **Chapter 6 - Validation of Accuracy using Radioactive Microspheres**

To assess the accuracy of the MBF measurements, a microsphere method was developed based on previous published methods and surgical feasibility. The following chapter describes the method development and results from these more invasive, terminal microsphere procedures and outlines some of the difficulties encountered.

### **6.1 - Theory**

Microsphere studies are invasive, terminal procedures in which  $\mu\text{m}$ -sized polystyrene spheres are injected into the bloodstream and lodge in the capillary beds in proportion to blood flow. Microspheres measure absolute blood flow in units of  $\text{ml}/\text{min}/\text{g}$ . The general technique involves injecting an appropriate number of well-mixed microspheres into the blood, upstream of the organ of interest. If suitably sized, the microspheres travel through the arterioles and become lodged in the capillary bed in proportion to blood flow. The organ of interest is then excised and weighed followed by subsequent microsphere quantification using radioactive, optical or fluorescence methods. The number of microspheres present in the excised tissue is normalized by a reference blood sample taken at the time of microsphere injection. This reference blood sample is taken at a known withdrawal rate and is used to normalize the measured microspheres into absolute units of flow in terms of  $\text{ml}/\text{min}/\text{g}$ . The equation for measuring regional blood flow (RBF) using radioactive microspheres is given by,

$$RBF = \frac{S_i R_r}{R_a} \quad (6.1)$$

where  $S_i$  are the counts obtained in the tissue piece  $i$  in units of counts/g,  $R_r$  is the reference withdrawal rate in units of ml/min, and  $R_a$  is the counts obtained in the reference sample. In the case of all cardiac sections, RBF and MBF are equivalent.

In order to obtain accurate measurements using microspheres, there are many conditions that need to be satisfied. Firstly, adequate and uniform mixing prior to and after injection is essential for uniform distribution of microspheres in the circulatory system. Secondly, proper microsphere size must be carefully chosen as the entrapment of microspheres must occur during the first pass through the arterial blood without passing into the venous system. Finally, the microsphere injection cannot alter the physiology or hemodynamics of the subject or organ of interest. If all of these stipulations are met, adequate numbers of microspheres are injected, and careful techniques are adopted, microsphere measurements should provide accurate measurements of absolute blood flow.

## 6.2 - Literature Review

In the late 1960's and early 1970's, radioactive microspheres were developed as the standard marker for regional blood flow<sup>50</sup>. Since then, more data has been presented describing the technical development of the microsphere detection method as well as the optimization of parameters for microsphere studies in small animals.

Microspheres can be coloured, fluorescent or radioactively-labeled for detection and quantification<sup>50</sup>. Each type has its advantages and disadvantages. For example, fluorescent microspheres, have been shown to be a cost-effective, stable alternative to radioactively-labeled microspheres, reducing unnecessary exposure to radiation<sup>50</sup>. The disadvantage of fluorescent microspheres, however, is that tissue preparation prior to

quantification is much more labour intensive<sup>51</sup>. Both radioactively- and fluorescently-labeled microspheres have been shown to have similar accuracy in perfusion studies performed in rabbits<sup>52</sup> and can be used interchangeably. In this work, radioactive microspheres were chosen due to an accessible on-site gamma counter and an existing framework of radionuclide licensing.

Many groups have also investigated the size of the microspheres and its relation to the accuracy of the measurements, as well as how this affects the subject's physiology and hemodynamics. As mentioned previously, microspheres must be large enough to lodge in the capillary bed without changing the organ's global hemodynamics. Although it has been documented that regional blood flow measurements have been successfully made using 9-25  $\mu\text{m}$  diameter micropsheres<sup>53</sup>, the most common size for dogs<sup>53;54</sup>, sheep<sup>53</sup> and rats<sup>36;44;45;55</sup> are 15  $\mu\text{m}$ . Some groups, however, have reported that 15  $\mu\text{m}$  diameter microspheres are too large for specific studies on organs such as the rat eye in which they tended to lodge in pre-capillary arterioles and cause significant rises in blood pressure<sup>56</sup>.

Appropriate numbers of microspheres to inject is also an important issue of accuracy that has been studied extensively. It has been shown empirically that to reduce sources of error in the measurements, and to be 95% confident that the measurement is within 10% of the true value, a total of 400 discrete microspheres must be present in the final tissue section<sup>57</sup>. Therefore, to calculate the minimum number of microspheres to inject in order to satisfy this condition, the following equation is used<sup>58</sup>:

$$N = \frac{400n}{\left(\frac{F_{organ}}{F_{total}}\right)} \quad (6.2)$$

where  $N$  is the minimum number of microspheres needed in the injection,  $n$  is the number of organ sections and  $F_{organ}/F_{total}$  is the fraction of cardiac output supplying the organ of interest. Although the minimum number of microspheres that can be injected is a guideline, it has been shown that increasing the number of microspheres injected well above this minimum value has low risk for obstructive, hemodynamic effects in rats<sup>59</sup>.

Typically, microspheres have a tendency to aggregate together. Apart from the methodological solutions such as ultrasonification, vortexing, and mixing by pipette, a surfactant is usually added to the solution to minimize aggregation. This surfactant is usually Polysorbate-80 or more commonly known as Tween-80. Previous reports in rats indicate that Tween-80 may have a hypotensive effect<sup>60</sup> and should be accompanied by an infusion of intravenous fluid during both the microsphere injection and the blood withdrawal procedure.

Varying the location for microsphere injection and blood withdrawal has also been attempted. In order to obtain optimal mixing, it is important to inject as high as possible upstream in the circulation. For example, for cardiac studies, it is ideal to inject in the left atrium to achieve mixing prior to entering the LV cavity. Atrial injections are technically challenging in small animals, therefore LV injections have been performed reportedly with no loss in accuracy. In the study by Schrock *et al.*<sup>45</sup>, it was shown that there was no difference in accuracy between a left atrial and a left ventricular injection in rats. In 1998, Shimada *et al.*<sup>61</sup> injected 15  $\mu$ m microspheres through a catheter inserted via the right carotid artery advanced into the LV of a rabbit. A reference blood sample was then withdrawn from the femoral artery. In rats, various sites of injection have been used including entrance through the thoracic cavity, directly into the LV<sup>36</sup> as well as

through the right carotid artery into the LV<sup>45;55</sup>. The most common blood withdrawal site in rats is the femoral artery<sup>53;55;61</sup>. Accuracy has also been achieved using the descending aorta<sup>36</sup> and the tail artery for blood withdrawal<sup>45</sup>. Blood withdrawal rates in rats from these studies range from 0.5-0.8 ml/min.

Based on previously published data, a microsphere protocol was developed for in-house use. The next section describes the surgical and data acquisition methods used in this study for validating myocardial blood flow with microspheres.

### 6.3 - Surgical and Data Acquisition Methods

In order to carry out invasive measurements of MBF on 18 rats, 15  $\mu\text{m}$  diameter <sup>141</sup>Ce-radiolabeled microspheres suspended in 0.01% Tween-80 and normal saline (Perkin Elmer Product Code NEM022A) were used. Cerium-141 has a 32.53 day half-life and decays by beta emission with a principle gamma energy of 0.145 MeV<sup>62</sup>. Quality assurance was carried out by the manufacturer before shipment of microspheres as described by previous methods<sup>63</sup>. The microspheres had a mean  $\pm$  SD size of  $15.5 \pm 0.1 \mu\text{m}$ , a specific activity of 1408.9 MBq/g and a concentration of  $1.19 \times 10^6$  beads/ml in 4.0 ml. The microspheres were stored at 4°C in lead shielding. Following removal from the 4°C refrigerator, the supernatant was inspected for clarity as a cloudy supernatant could indicate contamination. Prior to surgery, the suspension was mixed by ultrasonification for 2 min followed by vortexing for 1 min and mixing by pipetting for 30 sec to uniformly re-suspend any settled microspheres. In order to inject approximately  $1.3 \times 10^5$  microspheres into each animal following previously published protocols, a total volume of 115  $\mu\text{l}$  was required. Aliquots of solution were measured into glass vials and left until injection.

During the surgery, the rats were anesthetised using 2%-2.5% isoflurane via an induction chamber and a subsequent nose cone maintaining 2% isoflurane throughout the procedure. A tail vein catheter was inserted into one of the two tail veins. The tail vein catheter was capped and taped to the rat's tail for easy IV injection of radiotracer. To troubleshoot the microsphere method, multiple locations were used for microsphere injection and reference blood sample withdrawal. In the first group, a catheter was placed through the carotid artery and down into the left ventricle for microsphere injection using PE50 tubing (internal diameter=0.58 mm). For reference blood withdrawal, a catheter was placed in the femoral artery using PE10 tubing (internal diameter=0.28 mm) attached to an automatic blood sampler and syringe pump<sup>64</sup>. In the second group, a reference blood sample was taken by placing a catheter in the carotid artery using PE50 tubing attached to an automatic blood sampler and syringe pump. For microsphere injection, a small thoracic incision was made in the skin and a 30 gauge needle with PE10 tubing attached was inserted between 3rd and 4th rib directly into the LV. The correct location of the needle was obvious due to its synchronous movement with the rat's cardiac rhythm, and by the ease of withdrawing blood from the LV cavity. Body temperature and respiration rate were monitored via the monitoring system described in Section 5.1 and body temperature was maintained using a heating pad set to 34°C or 36°C. After ensuring that the monitoring devices were functional, the rat was stable and the microsphere suspension was ready and well-mixed by an additional vortexing step, the reference blood sampler was started at a rate of 0.5 ml/min for 2 min to obtain a 1.0 ml blood sample. Once the blood sampler had started its withdrawal, the PET scanner was immediately started. Approximately 10 seconds after starting the PET

scanner, the 115  $\mu\text{l}$  aliquot of microsphere suspension was injected into the LV cavity simultaneously with 75-150 MBq of  $^{13}\text{N}$ -ammonia into the tail vein over an approximate 6 second span (approximately 1.0 ml/min). Following the injection, approximately 100-200  $\mu\text{l}$  of 0.9% saline was injected to flush both the microsphere and radiotracer catheters of any remaining activity. List-mode data was acquired for 30 min using a 350-650 keV energy window and a timing window of 3.432 ns for subsequent MBF analysis.

Following completion of the scan, the rat was euthanized according to animal care protocols and the heart was excised along with a section of the superior lobe of the liver (consistent between all animals) and both kidneys. To check for adequate microsphere mixing in the aorta, the activity in the left and right kidneys should agree to within 10%<sup>44</sup>. Data in animals failing this requirement were rejected from the analysis. Taking note of the LV orientation, the atria and RV were carefully removed from the heart. The LV was dissected into five sections (anterior, posterior, septal, lateral and apex) corresponding to the PET imaging polar map representation. The sections were placed in clean, pre-weighed tubes for gamma counting. The activity of the reference blood sample, reference blood syringe, reference catheter, and all tissue samples were counted using a Cobra gamma counter for 2 min/sample to ensure 1% uncertainty or 10,000 counts per sample.

#### 6.4 - Results

Using the condition that flow in the left and right kidneys must be in agreement by less than 10%, 7 of the 18 animals were rejected from analysis due to inadequate microsphere mixing. A table summarizing the results from the microsphere studies is shown in Table 6.1 where MBF-MS is the microsphere derived value for MBF and where

MBF-PET is the PET derived value for MBF. PET data for Rats 3 and 6 are omitted due to tracer injection problems as no usable PET data was acquired. The CV values shown in Table 6.1 correspond to the MBF-MS values across all five segments of the LV.

**Table 6.1 Summary table of microsphere results**

Rat ID	MBF-MS Myocardium (ml/min/g)	CV (%)	MBF-PET Myocardium (ml/min/g)	MBF-MS Kidney Difference (%)
1*	7.8	11.0	4.6	1.7
2*	15.8	23.1	5.7	1.3
3*	22.2	34.7	-	5.3
6#	12.4	13.3	-	6.8
7#	25.3	10.2	6.3	5.7
8#	2.3	37.4	6.4	9.0
12#	5.3	12.8	4.0	1.8
14#	14.7	24.2	6.1	7.1
15#	1.1	10.6	5.5	6.6
16*	25.3	50.9	6.2	6.0
17*	11.5	62.6	4.8	4.0

\* denotes an LV injection through the carotid artery, # denotes an direct intercostal injection into the LV

Apparent from Table 6.1, and in all cases but two (rats 8 and 15), the microsphere derived values of MBF are significantly higher and much more variable than the PET derived values. Figure 6.1 illustrates the severe overestimation in MBF using microspheres versus PET as well as the large variability in microsphere measurements. If the two methods were in perfect agreement, data points should fall on the black line.

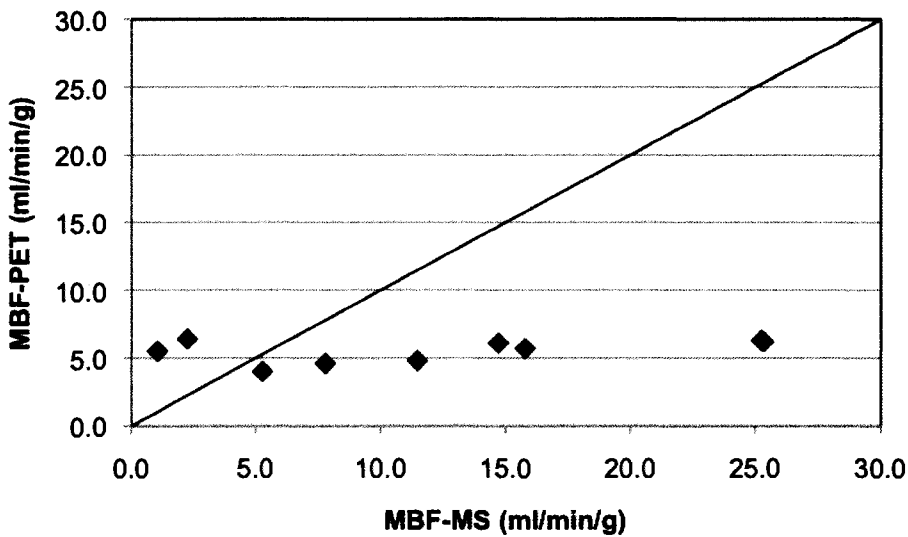


**Figure 6.1**  $^{13}\text{N}$ -ammonia PET derived MBF values (MBF-PET) versus microsphere derived MBF values (MBF-MS). The black line indicates a perfect agreement between methods

Since microspheres are an established method for validating flow measurements, the erroneous results obtained in this study are attributable to methodology alone and are in no way taken to be a significant finding. Previous reports describing the use of microspheres to study MBF in rats quote values ranging from 3.65 - 8.58 ml/min/g in normal rats under isoflurane anaesthetic<sup>36;44;45</sup>. Difficulty establishing a reproducible microsphere method is common due to its technically demanding protocol and surgical procedures. In 1977, ten years following the discovery of particulate microspheres, Heymann *et al.*<sup>63</sup> quoted that, “poor techniques and inattention to detail may result in inaccurate and misleading results”. Using microspheres in rats, McDevitt *et al.*<sup>55</sup> do not provide any data for perfusion in the heart admitting that the potential for errors in the heart would be high relative to other organs. More recently, Croteau *et al.*<sup>30</sup> admit that a current limitation of the study is the lack of a gold standard for MBF even after extensively studying rat MBF under anaesthesia. Some other published experiments even

quote that their microsphere results were unreliable and non-reproducible<sup>65</sup>. For the remainder of this chapter, the results obtained, and possible alterations to the method will be discussed.

Also shown in Table 6.1 are the CV values for each heart across the five segments. Although the absolute LV means are mostly outside normal ranges, a low CV value indicates that there is good uniformity across the LV. Compared to the mean CV in PET derived MBF polar maps (shown to be 17% in Chapter 5), a small subset of rats (rats 1, 6, 7, 12, and 15) surprisingly have better regional uniformity (11, 13, 10, 13 and 11% respectively). This would suggest that there was adequate mixing and proper microsphere deposition in this subset. The problem, however, seemed to be that the reference blood withdrawal was not accurate since this is the measurement that normalizes the tissue data into units of ml/min/g. Of the 11 rats used in the analysis, 9 seemed to have been overestimated, also indicating that the reference blood sample was likely erroneous. This overestimation could be the result of the failure to collect and quantify all of the microspheres in the reference blood sample, driving the MBF value up as shown in Equation 6.1. To correct for this problem, all surgical catheters, syringes and tubing used for the blood collection were counted using the gamma counter, however, only a negligible amount of microspheres were found, and these did not significantly affect the measured MBF values.

In order to troubleshoot the microsphere injection and withdrawal, as mentioned in the methods (Section 6.3), two different locations were used for both the injection and withdrawal. The first method was to inject through a catheter in the carotid artery advanced down into the LV and withdraw blood from the femoral artery. The second

method was to inject directly into the LV using a needle inserted through the rib cage and withdraw from the carotid artery. The first method proved to be more technically challenging and based on the results obtained shown in Table 6.1, neither method improved the variability of the measurements.

## 6.5 - Conclusion

The validation of absolute MBF using microspheres was not successful as was evident from the results. Although an extensive literature search on methodology was carried out and careful attention was paid to detail, microspheres severely overestimated MBF as compared to published microsphere derived values as well as the image derived values in this study. A subset of rats in this study exhibited extremely uniform MBF across the LV, with smaller CV values than the population mean CV investigated in Chapter 5. This uniformity suggests that there was adequate mixing and uniform deposition in the tissue but an improper normalization due to an incorrect reference blood sample. Efforts were made to improve the accuracy of the blood sample by including all tubes, catheters and syringes in the gamma counting stage without success. Other variations of the surgical method included using different injection techniques such as direct LV injection as well as various injection and withdrawal locations. These modifications proved to have no impact on improving the variability or accuracy of the microsphere methods. Although challenging, further investigation into the method of the described microsphere technique would be necessary in order to obtain accurate, reproducible measurements of MBF using microspheres to validate the PET derived values.

## **Chapter 7 - Rat Myocardial Blood Flow Outside Normal Ranges: Infarct Model**

In Chapter 5, the relative and absolute MBF measurements of a normal population were presented. In this chapter, an infarct rat model was used in order to test the accuracy of detecting disease using the developed imaging and analysis methods by comparing against the established normal population.

A rat infarct model uses a rat that has undergone a surgical procedure in which one or more coronary vessels were surgically occluded to mimic an acute, non-fatal myocardial infarction (MI), also known as a heart attack.

### **7.1 - Methods**

Myocardial infarction was created in three Sprague Dawley rats by ligating (surgically tying off) the LAD artery. This procedure was performed by Charles River Canada prior to delivery of the animals to the University of Ottawa Heart Institute. Upon receipt, the rats weighed between 150-175 g and were housed at an ambient temperature with water and food provided *ad libitum*.

All infarct rats were scanned 9 weeks post-MI where 8-9 weeks represented end-stage heart failure according to the supplier as assessed by low LVEF. Euthanasia was conducted immediately after the week 9 post-MI scan according to internal animal care guidelines. All data presented in this chapter originates from the three rats at week 9 post-MI (mass = 450-500 g).

The experimental protocol for data acquisition was similar to that previously described in Section 5.1. Attenuation and scatter corrections were not incorporated into the reconstructions, however, a 10 min transmission image was acquired for future reference. The resulting images were subjected to semi-automated analysis using FlowQuant<sup>©</sup> to generate polar maps of <sup>13</sup>N-ammonia uptake and absolute MBF as per Section 5.1.

To construct the uptake and MBF polar maps used in detecting disease, mean and standard deviation polar maps were generated on a sector-by-sector basis using the polar maps of the normal population presented in Chapter 5. Any sector in the infarct rat scan that had a value outside the normal range as defined by the mean minus 2SD was highlighted.

## 7.2 - Results

Analysis of the <sup>13</sup>N-ammonia uptake and MBF polar maps revealed evidence of disease. Figure 7.1 illustrates both the uptake (A) and MBF (B) polar maps for Rats 1-3.

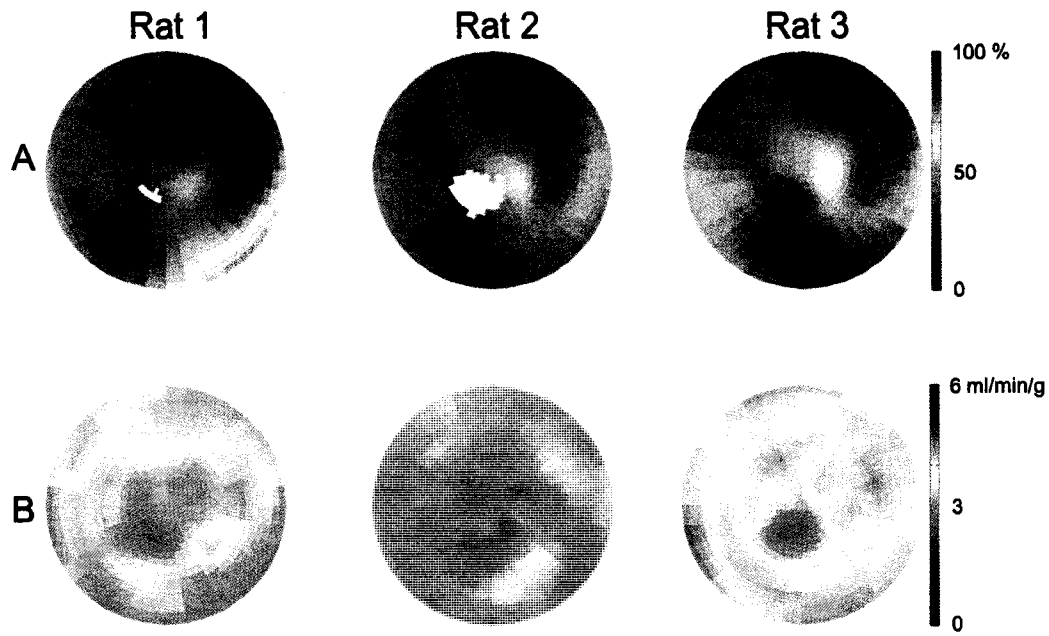


**Figure 7.1**  $^{13}\text{N}$ -ammonia uptake (A) and MBF (B) polar maps from the three infarct rats

In the uptake polar maps shown in Figure 7.1A, all three rats show regions of moderately decreased perfusion relative to the normal anterolateral wall. These regions of approximately 60-75% uptake include the posterolateral, apical and septal walls. Although the anterior wall is mainly supplied by the LAD<sup>66</sup>, no decrease in  $^{13}\text{N}$ -ammonia uptake was observed in this region, contrary to what was expected.

Although relative perfusion imaging is important in determining regions of low blood flow relative to a normal region within the LV, one limitation is that it cannot detect global changes in MBF. These global changes could be due to multi-vessel disease or differences in weight/age as shown in Chapter 5. Figure 7.1B shows the absolute MBF polar maps from the same infarct rats. These maps are displayed using the same scale as all previous MBF measurements for comparison. Evident from these polar maps, there is a decrease in global perfusion in all three rats as compared to the mean normal

MBF of  $5.73 \pm 0.94$  ml/min/g in this weight group ( $>400$  g). Also apparent are regional reductions in perfusion similar to those observed in the uptake maps in the posterolateral and apical walls. The septal walls in rats 1 and 2 also exhibit decreased perfusion.

To detect regional defects in flow quantitatively, the databases of normal uptake and absolute MBF values presented in Chapter 5 can be employed. Due to the absolute MBF increase with weight presented in Chapter 5, a certain subset of data needed to be chosen to match the diseased subjects weight of 450-500 g. The subset chosen were the 6 normal subjects  $>400$  g (Figure 5.7 or referred to Group 1 in Section 5.6, Table 5.4 and Figure 5.11). By constructing mean and SD polar maps of the 6 normal rats on a sector-by-sector basis, it was possible to locate all sectors on the infarct polar maps that had a value below 2SD of the normal uptake and MBF ranges as shown in Figure 7.2. The global mean minus 2SD cut-off values for uptake and MBF were 77.3% and 2.40 ml/min/g respectively. All abnormal regions detected are indicated by dark blue sectors and all apical sectors of the uptake maps that have been cropped are indicated by light green sectors.

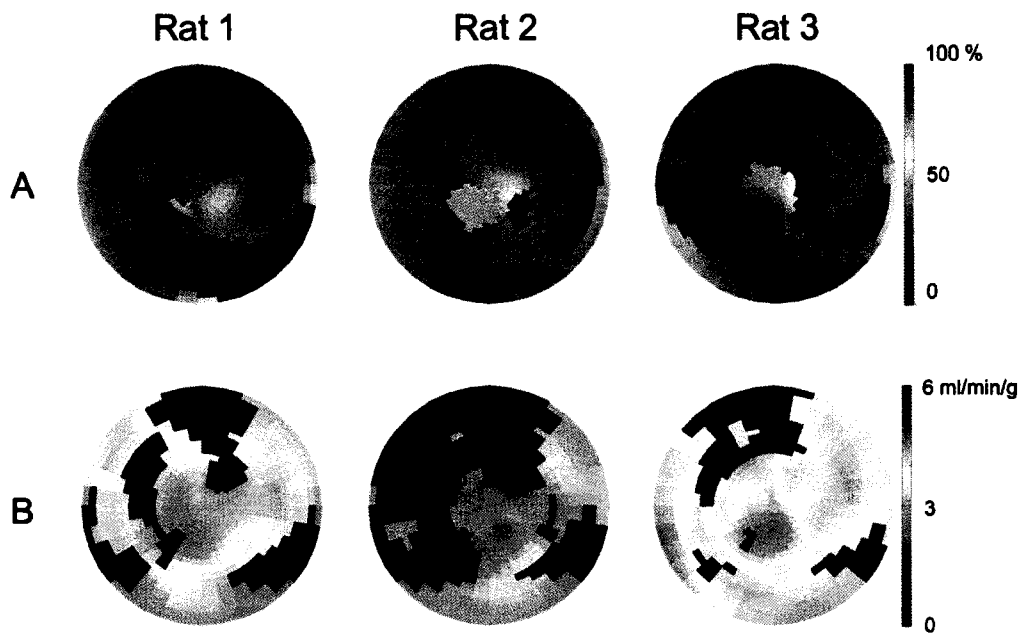


**Figure 7.2 Regions identified as abnormal in Rats 1-3 using A) uptake and B) MBF polar maps. Dark blue colour indicates an abnormal sector as assessed by having a value outside the normal range of the sector mean - 2SD. Light green regions in the apical regions of the uptake maps indicate cropped sectors**

The larger extent of the Rat 2 infarct is more apparent from Figure 7.2B than it is from Figure 7.2A. This is attributable to the lower global MBF value as indicated by 7.1B and therefore more chance that each sector will fall below the mean minus 2SD range.

Also evident from Figure 7.2, are the similar patterns of the diseased regions identified when the uptake maps are complemented with the MBF maps, indicating abnormalities in the anteroseptal and posterolateral regions. These regions coincide very well with the regions supplied by the LAD and LCX in rats<sup>66</sup>. The LAD supplies the anterior, septal and apical (top, left and centre) regions, the LCX supplies the lateral (right) region, and in approximately 50% of the cases, the RCA supplies the posteroseptal (bottom left) region (See Figure 3.4). Otherwise, the left coronary artery (LAD and LCX)

supplies the entire left ventricle<sup>66</sup>. The largest area with decreased perfusion is the region supplied by the LAD which is consistent with the surgical ligation of the LAD.

Abnormal perfusion values were localized in the septal and posterolateral regions of the MBF polar maps (Figure 7.2B), consistent with the abnormal uptake shown (Figure 7.1A) and quantitatively detected (Figure 7.2A) in the relative polar maps. Interestingly, however, the method of using the absolute MBF database detected disease in the anteroseptal wall not shown on the relative map of Rat 2, and failed to detect the reduced perfusion in the apex shown on all of the relative and absolute polar maps. Although the uptake map of Rat 2 does not show significant regional variations, the absolute MBF of Rat 2 is globally reduced further justifying the use of the absolute MBF database to detect disease. The lack of abnormal tissue localized in the apex is a limitation of the method used. By using normal uptake and MBF databases with larger variability and consistently lower cut-off values in the apex, the threshold for detecting disease is increased.

### **7.3 - Conclusion**

The importance of an established database of normal MBF values in a population of rats was demonstrated to qualitatively and quantitatively localize global and regional abnormalities in infarct rats. The diseased regions located coincide with the expected regions supplied by the coronary arteries further indicating the diagnostic accuracy of the methods.

Based on the advantages of observing global changes in MBF using absolute perfusion measurements and the advantages of observing regional changes in relative

perfusion measurements, the data presented suggests that both methods should be employed when evaluating MBF in infarct rats.

This work has established proof-of-principle demonstrating that the imaging methods developed, the clinical analysis methods translated, and the normal perfusion results obtained, can quantitatively serve to detect and track both relative and absolute perfusion in rats *in vivo*.

## **Chapter 8 - Conclusions and Future Work**

The objective of this work was to develop and validate PET imaging methods for accurate and reproducible measurements of perfusion in rodent models of heart disease and to evaluate population variability and test-retest reproducibility within normal populations.

To accomplish this, many experiments were performed. Firstly, the scanner's stability was quantified over time using a daily protocol to ensure reproducible measurements throughout the duration of the study. Secondly, suitable reconstruction and analysis parameters were established for use in rat cardiac studies such as the optimization of the blood sampling volume and image zoom.

Once the preliminary objectives of translating clinical imaging techniques down to small animals had been successfully demonstrated, rat perfusion was studied on relative and absolute scales. A normal database consisting of 21 subjects was established exhibiting a relative perfusion population variability of 4% and an MBF variability of 27%, consistent with previously published human populations. The advantage in absolute MBF measurements, however, is that a physiological measure of perfusion in units of ml/min/g can be obtained. Using the absolute MBF values, an increase in MBF was found to be correlated with either age or weight, and the regression equation between weight and resting MBF was found to be  $MBF = 0.95 + 0.010g$ . This newly documented finding in rats is consistent with previous reports of human MBF values at rest increasing with age, however, it should be confirmed with measured changes in RPP.

The test-retest reproducibility ( $\pm 12.7\%$ ), intra-observer repeatability ( $\pm 4.1\%$ ) and the inter-observer repeatability ( $\pm 6.6\%$ ) was quantified in a subset of normal rats and was found to be a small source of uncertainty in the measured MBF in comparison to the population variability. This indicates that the scanner produces reproducible images, that the MBF values obtained are minimally influenced by human intervention, and that the image analysis methods are robust.

A current limitation to this work is the lack of microsphere data to validate the measured values of MBF. Despite the unreliable data, a detailed protocol and surgical methods were established but require further investigation into the possible causes of the variable data obtained. The irreproducible data may be due to the method of blood withdrawal as a small subset of the data showed extremely uniform flow values across the five segments of the LV suggesting sufficient mixing. Further troubleshooting is required for the method of blood withdrawal.

Finally, the developed methods and analyses were tested on a rat model of disease. It was found that clinical, diagnostic protocols could be translated to small animals. In addition, by using a database of normal perfusion values, disease could be detected quantitatively. Further to this, as expected, the disease was localized in regions that coincide with the tissue supplied by the LAD artery.

Future work involves troubleshooting the existing microsphere protocol in order to validate the accuracy of the MBF measurements. Furthermore, successful adaptation of the existing rat imaging and analysis protocols to mouse studies using additional signal recovery techniques to account for the small dimensions of the mouse heart are necessary. Proposed techniques could involve the use of cardiac gating in order to obtain

a blood TAC at end-diastole to reduce spillover from the myocardium, and to obtain a myocardial TAC at end-systole to reduce partial volume losses. Once these methods are established for mouse cardiac PET imaging and normal perfusion values are obtained, it should be possible to measure myocardial perfusion in mouse models of human disease serially, non-invasively and *in vivo*, as demonstrated in rats.

## Appendix

Similar to an algebraic technique used by Lin *et al.*<sup>43</sup>, a set of equations were developed for the one compartment model to correct for spillover of radioactivity from the myocardium to the blood ( $S_{mb}$ ) in addition to the  $TBV$  vascular fraction correction described in Chapter 2. By defining a region of interest (ROI) in the myocardial tissue and LV blood cavity at any time  $t$ , the measured signals including spillover would be:

$$C_a'(t) = C_a(t) + S_{mb}C_m(t)(1-TBV) \quad (\text{A.1})$$

$$C_m'(t) = C_m(t)(1-TBV) + C_a(t)TBV \quad (\text{A.2})$$

where  $C_a'(t)$  and  $C_m'(t)$  are the measured blood and myocardial TACs respectively;  $C_a(t)$  and  $C_m(t)$  are the true blood and tissue TACs respectively; and  $(1-TBV)$  is the recovery coefficient to account for partial volume losses in the myocardium as described in Chapter 2. According to Equation A.1, the measured blood TAC would include the true blood signal with additional signal from a fraction ( $S_{mb}$ ) of the measured tissue ( $C_m(t)(1-TBV)$ ). Similarly in Equation A.2, the measured tissue TAC would include the true tissue signal accounting for partial volume losses ( $C_m(t)(1-TBV)$ ) with additional signal from the vascular fraction of the blood signal ( $C_a(t)TBV$ ).

Using Equations A.1 and A.2 to eliminate  $C_m(t)(1-TBV)$ , the true blood TAC can be solved for:

$$C_a(t) = \frac{C_a'(t) - S_{mb}C_m'(t)}{1 - S_{mb}TBV} \quad (\text{A.3})$$

Similarly, using Equations A.1 and A.2 to eliminate  $C_b(t)$ , the true myocardium TAC can be solved for:

$$C_m(t) = \left( \frac{1}{1 - TBV} \right) \frac{C_a'(t) - (TBV)C_b'(t)}{1 - S_{mb}TBV} \quad (\text{A.4})$$

Evident from Equations A.3 and A.4, true TACs for both the blood and myocardium can be obtained using measured data ( $C_a'(t)$  and  $C_m'(t)$ ), a parametric estimate (TBV) and an additional estimate of myocardial spillover into the blood,  $S_{mb}$ . To get an estimate of  $S_{mb}$ , an assumption is made. This estimation assumes that the true activity in the blood,  $C_a(t)$ , is zero in the last time frame in the dynamic scan ( $t=25\text{-}30\text{min}$ ). This assumption can be taken as valid based on previous reports<sup>67</sup>. Using this assumption and Equation A.1,  $S_{mb}$  can be measured in the last time frame:

$$S_{mb} = \frac{C_a'}{C_m(1 - TBV)} \quad (\text{A.5})$$

or more clearly,

$$S_{mb} = \frac{C_a'}{C_m'} \quad (\text{A.6})$$

The algebraic spillover correction method developed in this appendix could provide additional contrast recovery between myocardial and blood TACs in the cases of small hearts and large amounts of spillover. It is recommended to apply this method on a sector-by-sector basis using sector values of TBV to obtain a more accurate TBV and RC correction.

## References

1. Lamoureux, M., Thorn, S., Klein, R., Lortie, M., Renaud, J., Beanlands, R. S., DaSilva, J. N., and deKemp, R. A. Quantification of myocardial blood flow in rat myocardium with N-13 ammonia and a new microPET scanner. *J Nucl Med.* 49 (Supplement 1):151P. 2008.  
Ref Type: Abstract
2. "The Changing Face of Heart Disease and Stroke in Canada," *Public Health Agency of Canada*, 2000.
3. "International Cardiovascular Disease Death Rates," *American Heart Association*, 2007.
4. *Positron Emission Tomography of the Heart*, ed. S. R. Bergmann and B. E Sobel. (Mount Kisco, NY: Futura Publishing Company, Inc., 1992).
5. T. D. Ruddy, R. A. deKemp, and R. S. Beanlands, "Taking PET to Heart," *CMAJ.* 161, no. 9 (1999): 1131.
6. S. R. Cherry and M. Dahlbom, "PET: Physics, Instrumentation, and Scanners," in *PET: Molecular Imaging and Its Biological Applications*, ed. M. Phelps. (New York: Springer-Verlag, 2004), 1-124.
7. G. F. Knoll, *Radiation Detection and Measurement* Second ed. (New York: John Wiley & Sons, 1989).
8. H. E. Johns and J. R. Cunningham, *The Physics of Radiology* Fourth ed. (Springfield, Illinois: Charles C Thomas, 1983).
9. C. C. Watson et al., "Evaluation of Simulation-Based Scatter Correction for 3-D PET Cardiac Imaging," *IEEE Trans Nucl.Sci.* 44 (1997): 90-97.
10. J. L. Prince and J. M. Links, *Medical Imaging Signals and Systems* (Upper Saddle River, New Jersey: Pearson Prentice Hall, 2006).
11. R. E Carson, "Tracer Kinetic Modeling in PET," in *Positron Emission Tomography*, ed. D. L. Bailey et al. (London: Springer-Verlag, 2005), 127-159.
12. R. A. deKemp, K. Yoshinaga, and R. S. Beanlands, "Will 3-Dimensional PET-CT Enable the Routine Quantification of Myocardial Blood Flow?," *J Nucl Cardiol* 14, no. 3 (2007): 380-397.

13. G. D. Hutchins, J. M. Caraher, and R. R. Raylman, "A Region of Interest Strategy for Minimizing Resolution Distortions in Quantitative Myocardial PET Studies," *J Nucl Med.* 33, no. 6 (1992): 1243-1250.
14. M. D. Cerqueira et al., "Standardized Myocardial Segmentation and Nomenclature for Tomographic Imaging of the Heart: a Statement for Healthcare Professionals From the Cardiac Imaging Committee of the Council on Clinical Cardiology of the American Heart Association," *Circulation* 105, no. 4 (2002): 539-542.
15. A. C. Guyton and J. E. Hall, *Textbook of Medical Physiology* Tenth ed. (Philadelphia: W.B. Saunders Company, 2000).
16. H. Schelbert, "Positron Emission Tomography of the Heart: Methodology, Findings in the Normal and Diseased Heart, and Clinical Applications," in *PET: Molecular Imaging and Its Biological Applications*, ed. M. Phelps. (New York: Springer-Verlag, 2004), 389-508.
17. H. Schoder et al., "Blood Flow-Metabolism Imaging With Positron Emission Tomography in Patients With Diabetes Mellitus for the Assessment of Reversible Left Ventricular Contractile Dysfunction," *J Am.Coll.Cardiol* 33, no. 5 (1999): 1328-1337.
18. J. Tillisch et al., "Reversibility of Cardiac Wall-Motion Abnormalities Predicted by Positron Tomography," *N.Engl.J Med.* 314, no. 14 (1986): 884-888.
19. Dahl J. vom et al., "Relation of Regional Function, Perfusion, and Metabolism in Patients With Advanced Coronary Artery Disease Undergoing Surgical Revascularization," *Circulation* 90, no. 5 (1994): 2356-2366.
20. S. R. Bergmann et al., "Noninvasive Quantitation of Myocardial Blood Flow in Human Subjects With Oxygen-15-Labeled Water and Positron Emission Tomography," *J Am.Coll.Cardiol* 14, no. 3 (1989): 639-652.
21. S. Y. Chan et al., "Comparison of Maximal Myocardial Blood Flow During Adenosine Infusion With That of Intravenous Dipyridamole in Normal Men," *J Am.Coll.Cardiol* 20, no. 4 (1992): 979-985.
22. J. Czernin et al., "Influence of Age and Hemodynamics on Myocardial Blood Flow and Flow Reserve," *Circulation* 88, no. 1 (1993): 62-69.
23. G. D. Hutchins et al., "Noninvasive Quantification of Regional Blood Flow in the Human Heart Using N-13 Ammonia and Dynamic Positron Emission Tomographic Imaging," *J Am.Coll.Cardiol* 15, no. 5 (1990): 1032-1042.

24. E. Tadamura et al., "Comparison of Myocardial Blood Flow During Dobutamine-Atropine Infusion With That After Dipyridamole Administration in Normal Men," *J Am. Coll. Cardiol* 37, no. 1 (2001): 130-136.
25. I. Yokoyama et al., "Impaired Myocardial Vasodilation During Hyperemic Stress With Dipyridamole in Hypertriglyceridemia," *J Am. Coll. Cardiol* 31, no. 7 (1998): 1568-1574.
26. J. Krivokapich et al., "13N Ammonia Myocardial Imaging at Rest and With Exercise in Normal Volunteers. Quantification of Absolute Myocardial Perfusion With Dynamic Positron Emission Tomography," *Circulation* 80, no. 5 (1989): 1328-1337.
27. R. S. Beanlands et al., "Heterogeneity of Regional Nitrogen 13-Labeled Ammonia Tracer Distribution in the Normal Human Heart: Comparison With Rubidium 82 and Copper 62-Labeled PTSM," *J Nucl Cardiol* 1, no. 3 (1994): 225-235.
28. M. J. Senneff, E. M. Geltman, and S. R. Bergmann, "Noninvasive Delineation of the Effects of Moderate Aging on Myocardial Perfusion," *J Nucl Med.* 32, no. 11 (1991): 2037-2042.
29. N. G. Uren et al., "Effect of Aging on Myocardial Perfusion Reserve," *J Nucl Med.* 36, no. 11 (1995): 2032-2036.
30. E. Croteau et al., "Quantitative Myocardial Perfusion and Coronary Reserve in Rats With 13N-Ammonia and Small Animal PET: Impact of Anesthesia and Pharmacologic Stress Agents," *J.Nucl.Med.* 45, no. 11 (2004): 1924-1930.
31. F. Kober et al., "Myocardial Blood Flow Mapping in Mice Using High-Resolution Spin Labeling Magnetic Resonance Imaging: Influence of Ketamine/Xylazine and Isoflurane Anesthesia," *Magn Reson.Med.* 53, no. 3 (2005): 601-606.
32. I. Iltis et al., "Noninvasive Characterization of Myocardial Blood Flow in Diabetic, Hypertensive, and Diabetic-Hypertensive Rats Using Spin-Labeling MRI," *Microcirculation.* 12, no. 8 (2005): 607-614.
33. I. Iltis et al., "In Vivo Assessment of Myocardial Blood Flow in Rat Heart Using Magnetic Resonance Imaging: Effect of Anesthesia," *J Magn Reson.Imaging* 22, no. 2 (2005): 242-247.
34. I. Iltis et al., "Defective Myocardial Blood Flow and Altered Function of the Left Ventricle in Type 2 Diabetic Rats: a Noninvasive in Vivo Study Using Perfusion and Cine Magnetic Resonance Imaging," *Invest Radiol.* 40, no. 1 (2005): 19-26.

35. C. Waller et al., "Myocardial Perfusion and Intracapillary Blood Volume in Rats at Rest and With Coronary Dilatation: MR Imaging in Vivo With Use of a Spin-Labeling Technique," *Radiology* 215, no. 1 (2000): 189-197.
36. P. Herrero et al., "Assessment of Myocardial Blood Flow Using 15O-Water and 1-11C-Acetate in Rats With Small-Animal PET," *J.Nucl.Med.* 47, no. 3 (2006): 477-485.
37. R. Lecomte, "Technology Challenges in Small Animal PET Imaging," *Nuclear Instruments and Methods in Physics Research Section A* 527, no. 1-2 (2004): 157-165.
38. M. J. Raher et al., "In Vivo Characterization of Murine Myocardial Perfusion With Myocardial Contrast Echocardiography: Validation and Application in Nitric Oxide Synthase 3 Deficient Mice," *Circulation* 116, no. 11 (2007): 1250-1257.
39. Y. Yang et al., "Cardiac PET Imaging in Mice With Simultaneous Cardiac and Respiratory Gating," *Phys.Med.Biol.* 50, no. 13 (2005): 2979-2989.
40. T. Kudo et al., "Noninvasive Measurement of Myocardial Activity Concentrations and Perfusion Defect Sizes in Rats With a New Small-Animal Positron Emission Tomograph," *Circulation* 106, no. 1 (2002): 118-123.
41. M. J. Welch et al., "Assessment of Myocardial Metabolism in Diabetic Rats Using Small-Animal PET: a Feasibility Study," *J.Nucl.Med.* 47, no. 4 (2006): 689-697.
42. T. Dumouchel, "Performance evaluation and correction for scatter and attenuation on the LabPET4(TM) positron emission tomography system" (M.Sc.Carleton University, 2007).
43. K. P. Lin et al., "Correction of Spillover Radioactivities for Estimation of the Blood Time-Activity Curve From the Imaged LV Chamber in Cardiac Dynamic FDG PET Studies," *Phys.Med.Biol.* 40, no. 4 (1995): 629-642.
44. B. Debaene et al., "Effects of Ketamine, Halothane, Enflurane, and Isoflurane on Systemic and Splanchnic Hemodynamics in Normovolemic and Hypovolemic Cirrhotic Rats," *Anesthesiology* 73, no. 1 (1990): 118-124.
45. G. D. Schrock, R. L. Krahmer, and J. L. Ferguson, "Coronary Flow by Left Atrial and Left Ventricular Microsphere Injection in the Rat," *Am.J.Physiol* 259, no. 2 Pt 2 (1990): H635-H638.

46. E. J. Eisen, "Results of Growth Curve Analyses in Mice and Rats," *J Anim Sci.* 42, no. 4 (1976): 1008-1023.
47. J. M. Bland and D. G. Altman, "Statistical Methods for Assessing Agreement Between Two Methods of Clinical Measurement," *Lancet* 1, no. 8476 (1986): 307-310.
48. P. Chareonthaitawee et al., "Reproducibility of Measurements of Regional Myocardial Blood Flow in a Model of Coronary Artery Disease: Comparison of H<sub>2</sub>15O and <sup>13</sup>NH<sub>3</sub> PET Techniques," *J.Nucl.Med.* 47, no. 7 (2006): 1193-1201.
49. S. Nagamachi et al., "Reproducibility of Measurements of Regional Resting and Hyperemic Myocardial Blood Flow Assessed With PET," *J Nucl Med.* 37, no. 10 (1996): 1626-1631.
50. F. W. Prinzen and J. B. Bassingthwaighe, "Blood Flow Distributions by Microsphere Deposition Methods," *Cardiovasc.Res.* 45, no. 1 (2000): 13-21.
51. M. F. Van Oosterhout et al., "Fluorescent Microspheres to Measure Organ Perfusion: Validation of a Simplified Sample Processing Technique," *Am.J Physiol* 269, no. 2 Pt 2 (1995): H725-H733.
52. M. F. Van Oosterhout et al., "Fluorescent Microspheres Are Superior to Radioactive Microspheres in Chronic Blood Flow Measurements," *Am.J Physiol* 275, no. 1 Pt 2 (1998): H110-H115.
53. J. Utley et al., "Total and Regional Myocardial Blood Flow Measurements With 25 Micron, 15 Micron, 9 Micron, and Filtered 1-10 Micron Diameter Microspheres and Antipyrine in Dogs and Sheep," *Circ.Res.* 34, no. 3 (1974): 391-405.
54. B. C. Chen et al., "A New Noninvasive Quantification of Renal Blood Flow With N-13 Ammonia, Dynamic Positron Emission Tomography, and a Two-Compartment Model," *J.Am.Soc.Nephrol.* 3, no. 6 (1992): 1295-1306.
55. D. G. McDevitt and A. S. Nies, "Simultaneous Measurement of Cardiac Output and Its Distribution With Microspheres in the Rat," *Cardiovasc.Res.* 10, no. 4 (1976): 494-498.
56. L. Wang et al., "Microspheres Method for Ocular Blood Flow Measurement in Rats: Size and Dose Optimization," *Exp.Eye Res.* 84, no. 1 (2007): 108-117.

57. G. D. Buckberg et al., "Some Sources of Error in Measuring Regional Blood Flow With Radioactive Microspheres," *J Appl. Physiol* 31, no. 4 (1971): 598-604.
58. F. W. Prinzen and R. W. Glenny, "Developments in Non-Radioactive Microsphere Techniques for Blood Flow Measurement," *Cardiovasc. Res.* 28, no. 10 (1994): 1467-1475.
59. K. A. Stanek et al., "Hemodynamic Disturbances in the Rat As a Function of the Number of Microspheres Injected," *Am. J. Physiol* 245, no. 6 (1983): H920-H923.
60. K. A. Stanek et al., "Two Hemodynamic Problems Commonly Associated With the Microsphere Technique for Measuring Regional Blood Flow in Rats," *J Pharmacol. Methods* 13, no. 2 (1985): 117-124.
61. K. Shimada et al., "High-Resolution Cardiac PET in Rabbits: Imaging and Quantitation of Myocardial Blood Flow," *J. Nucl. Med.* 39, no. 12 (1998): 2022-2027.
62. J. T. Jones and E. N. Jensen, "Radiations From Cerium-141," *Physical Review* 97, no. 4 (1955): 1031-1033.
63. M. A. Heymann et al., "Blood Flow Measurements With Radionuclide-Labeled Particles," *Prog. Cardiovasc. Dis.* 20, no. 1 (1977): 55-79.
64. L. Convert et al., "A New Tool for Molecular Imaging: the Microvolumetric Beta Blood Counter," *J. Nucl. Med.* 48, no. 7 (2007): 1197-1206.
65. S. Wetterlin et al., "Studies on Methods for Determination of the Distribution of Cardiac Output in the Mouse," *Scand. J. Clin. Lab. Invest* 37, no. 5 (1977): 451-454.
66. S. H. Ahmed et al., "The Comparative Anatomy of the Blood Supply of Cardiac Ventricles in the Albino Rat and Guinea-Pig," *J. Anat.* 126, no. Pt 1 (1978): 51-57.
67. I. N. Weinberg et al., "Validation of PET-Acquired Input Functions for Cardiac Studies," *J. Nucl. Med.* 29, no. 2 (1988): 241-247.